A Rutherford backscattering study on radiation damage and the diffusion of krypton implanted into 6H-SiC

by

Chemist Mfanufikile Mabena

Submitted in partial fulfillment of the requirements for the degree of

MASTER OF SCIENCE (MSc)
in Physics

in the Faculty of Natural and Agricultural Sciences at the University of Pretoria

August……2014

Supervisor/Promoter: Prof. J.B. Malherbe

Co-supervisor: Dr. T.T. Hlatshwayo

A Rutherford backscattering study on radiation damage and the diffusion of krypton implanted into 6H-SiC

by

Chemist Mfanufikile Mabena

Submitted in partial fulfillment of the requirements for the degree of (MSc) in Physics in the Faculty of Natural and Agricultural Sciences, University of Pretoria

Supervisor/Promoter: Prof. J.B. Malherbe
Co-Supervisor: Dr. T.T. Hlatshwayo

A pebble bed modular reactor (PBMR) is a modern type high-temperature gas-cooled nuclear reactor (HTGR). The fuels of the PBMR are in the form of small multi-layered spheres called triple-coated isotropic (TRISO) particles. A key feature of this PBMR technology is the entrapment of the fission products (FPs) within the TRISO particles. Silicon carbide (SiC) is used as the main layer in the TRISO particles. Given the sophistication of the TRISO design the release of silver (Ag) has motivated a thorough investigation concerning the ability of SiC to entrap other fission products. In this project volume diffusion of Kr in 6H-SiC was investigated under the influence of radiation damage.

Kr (360 keV) ions were implanted into 6H-SiC at three different temperatures, i.e. room temperature, 350 ^{o}C and 600 ^{o}C, up to a fluence of 2×10^{16} ions/cm^{2}. The radiation damage retained after implantation was assessed with the Rutherford backscattering technique in the channelling mode (RBS-C). Annealing of radiation damage and diffusion of the implanted Kr were investigated during isochronal annealing in the temperature range 1000 – 1500 ^{o}C in steps of 100 ^{o}C for 5 hours using RBS-C and Rutherford backscattering spectroscopy (RBS), respectively.

The room temperature implantation amorphised the 6H-SiC to a depth of approximately 280 nm from the surface. This occurred because the thermal energy of the atoms at this temperature was not high enough to allow the displaced atoms to

recombine with their designated lattice positions. The high temperature implantations did not amorphise the 6H-SiC. The implantation at these temperatures did, however, cause a distortion of the 6H-SiC because of the defects and/or defect clusters that were retained. The 350 ^{o}C implantation retained a high damage density as compared to the 600 ^{o}C implantation. The reason for the decrease in damage density with increasing temperature can be explained in terms of the thermal energy available for the atoms to move around in the SiC. A high temperature implies a higher mobility of the atoms thus increasing the probability of the displaced atoms to recombine with their designated lattice positions. Consequently, a slight diffusion of the Kr was also observed at the high temperature implantations relative to the room temperature implantation. The Kr depth profiles were broader for the high temperature implantation. Implantation at different temperatures caused different degrees of retained radiation damage in the SiC, consequently, isochronal annealing was done to assess the recovery of the SiC and also the diffusion of the implanted Kr inside the SiC under the different conditions.

Epitaxial re-crystallisation from the amorphous-crystalline interface was observed after annealing the room temperature implanted sample at 1000 ^{o}C. However, no change in the Kr depth profile was observed after annealing at 1000 and 1100 ^{o}C for 5 hours. Annealing the same sample from 1100 to 1300 ^{o}C in steps of 100 ^{o}C for 5 hours did not result in any further epitaxial re-crystallisation. There, however, was a slight change of the SiC from the surface region at 1200 ^{o}C. The Kr depth profile started to broaden slightly at 1200 ^{o}C. An increased broadening was further observed at 1300 ^{o}C. In both instances the Kr depth profiles maintained an approximately Gaussian shape. This change in the Kr depth profile implies that there was Fickian type diffusion of the Kr at these temperatures. Annealing at 1400 ^{o}C resulted in a loss of about 30% of the Kr accompanied by a shift of the Kr depth profile towards the surface. These changes occurred simultaneously with the major epitaxial re-crystallisation of the SiC from the amorphous-crystalline interface. Further annealing at 1500 ^{o}C caused an additional loss of about 20% of the Kr accompanied by a pronounced shift towards the surface. This also occurred concurrently with the remarkable re-crystallization of the SiC. The Kr depth profile changes that occurred at 1400 and 1500 ^{o}C resulted in an asymmetric Kr profile and thus cannot be explained in terms of the Fickian diffusion process. The observed abrupt changes at 1400 and

1500 ^{o}C are consistent with the influence of thermal etching. This is because the thermal etching effect could have influenced the RBS spectrum and resulted in asymmetric depth profiles due the surface inhomogeneity.

Unlike in the room temperature implantation case where the thermal energy had to be enough to allow (1) excess defects to escape the disordered region; (2) provide sufficient mobility to allow atomic re-ordering, and finally (3) allow for the formation of appropriate bonds, in the high temperature case there was a consistent decrease in the retained damage with each annealing cycle. Through-out the annealing cycles the 350 ^{o}C implantation retained more damage than the 600 ^{o}C implantation. In all the annealing instances there was no observable change in the Kr depth profiles implying that no diffusion took place despite the re-ordering of the displaced host atoms. The stability of the Kr atoms in their implanted positions is a possible contributor to the resistance of the SiC from returning to its virgin crystalline structure as observed through the RBS-C spectrum. This is because the Kr atoms exist as point defects in the SiC lattice thus causing the de-channelling of the He ions as they penetrate the SiC. This, in addition to the de-channelling from the extended defects, caused an increased backscattering spectrum from the host atoms. Thorough-out the entire isochronal annealing experiments in the temperature range 1000 – 1500 ^{o}C the 6H-SiC retained all of the implanted Kr.

DECLARATION

I, Chemist Mfanufikile Mabena declare that the dissertation, which I hereby submit for the degree of MSc in Physics at the University of Pretoria is my own work and has not previously been submitted by me for a degree at this or any other tertiary institution.

Signature: ……

Date: ……

Acknowledgements

I would like to acknowledge the following people for their valuable contribution towards the completion of my MSc work:

- My academic promoters Prof. J.B Malherbe, and Dr. T.T. Hlatshwayo for the guidance and mentorship during this project.
- Fellow students in the physics department for the encouragement and moral support.
- My family for the moral support and patience (Kunini babuza ukuthi ngiceda nini): Linah Thabethe, Thandi Mabena, Dennis Mabena, Tumelo Mabena, Shaun Mabena, Faith Mabena, and Palesa Hlotse.
- My friends for the encouragement and believing in me (Namajita wase koneni sisonke magenge!).
- My high school teachers for believing in me. Especially Mr. Mphathi, my mathematics teacher in high school, your expertise and love for mathematics motivated many of us.
- God, for without the strength and mental capability this project would not be possible.
- The financial assistance of the NRF is hereby acknowledged. Opinions expressed and conclusions arrived at, are those of the authors and not to be necessarily attributed to the NRF.

TABLE OF CONTENTS

CHAPTER 1 INTRODUCTION

A pebble bed modular reactor (PBMR) is a modern type of high-temperature gas-cooled nuclear reactor (HTGR). In this HTGR the fuels are in the form of small multi-layered spheres called triple-coated isotropic (TRISO) particles. A key feature of this PBMR technology is the entrapment of the fission products (FPs) within the TRISO particles. The TRISO particle consists of a UO_2 core surrounded by four layers, which are all chemical vapour deposited (CVD). The inner layer of the TRISO particle consists of a porous carbon; followed by an inner pyrolytic carbon layer (IPyC); SiC and outer pyrolytic carbon layer (OPyC).

Silicon carbide (SiC) is a hard and strong material with good mechanical properties, and it has a low neutron capturing cross-section. These properties contribute to making SiC a potential cladding material for entrapping nuclear fission products. Further, SiC is a good material for the purpose outlined above since it has a low thermal expansion and high thermal conductivity. The combination of high thermal conductivity and low thermal expansion contribute to the outstanding thermal shock resistance of SiC. However, it has been reported that some of the FPs both gases (e.g. Kr and I) and solids (e.g. Ag) are released from the coated fuel particles under irradiation [Nic02][Xho11]. The release of Kr-85 from FPs may cause danger to personnel working in such reactor environments. Kr-85 is a FP that can cause serious skin problems, and lung damage to personnel involved if it is released. One of the possible migration paths of Kr out of the TRISO particles is diffusion. Therefore, the main objective of this project was to investigate the influence of radiation damage on the volume diffusion of Kr in SiC.

1.1 SILICON CARBIDE

1.1.1 CRYSTALLINE STRUCTURE

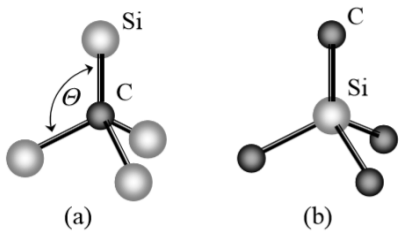

Figure 1.1: The basic unit of a SiC crystal. a) The C atom surrounded by four Si atoms, b) The Si atom surrounded by four C atoms. All atoms are bonded in a tetrahedral fashion. Figure taken from reference [Zol05].

A silicon carbide (SiC) crystal consists of 50% carbon (C) atoms and 50% silicon (Si) atoms. Each carbon atom is covalently bonded to four Si atoms (C-Si_4) and each Si atom is covalently bonded to four C atoms (Si-C_4). These covalent bonds occur in a tetrahedral fashion, as shown in figure 1.1. The short range order of a SiC crystal gives information about the chemical structure of the tetrahedron, and in a perfect SiC crystal it does not contain any homo-atomic bonds (Si-Si or C-C). Different crystals can be generated from the same basic tetrahedral unit of SiC. This is a property of crystals known as polytypism. There are over 200 known polytypes of SiC. All of these SiC polytypes have the same atomic arrangement in the plane perpendicular to the c-axis, whereas the stacking sequence of the SiC tetrahedral is different along the c-axis for each polytype. In the Ramsdell notation a SiC polytype is represented by a number and a letter. The number represents the number of bilayers, and the letter represents the crystal structure or Bravais lattice structure. Figure 1.2 shows two of the most common SiC polytypes, 4H-SiC and 6H-SiC. Each Si-C bilayer in figure 1.2 is represented by the dotted boxes. Each atom within the Si-C bilayer is bonded to three other atoms in the same layer, and with only one atom in the adjacent bilayer. In this project the 6H-SiC was used. A single crystal of 6H-SiC contains as its repeating unit 6 bilayers of Si and C atoms which have a hexagonal Bravais lattice

structure. The stacking sequence of the 6H-SiC crystal is given by ABCBAC, as shown in figure 1.2.

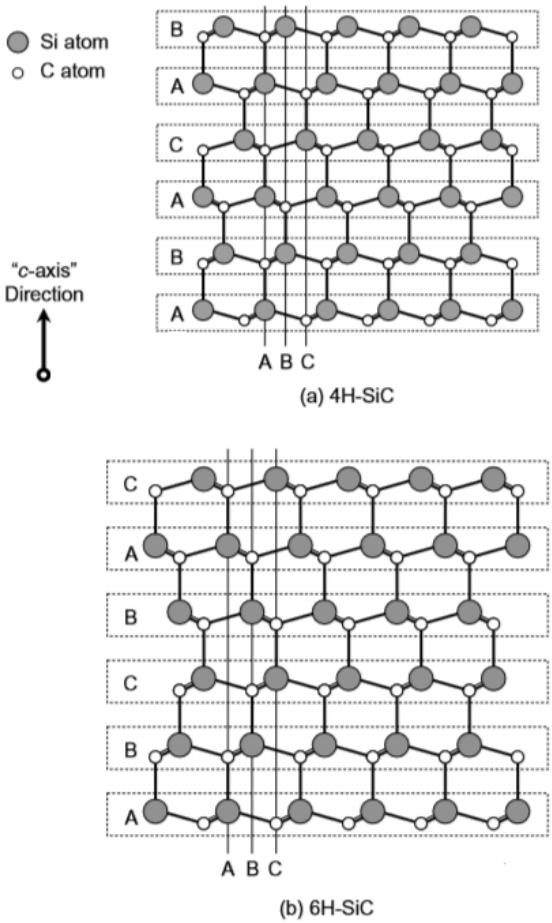

Figure 1.2: Schematic presentation of a) 4H-SiC in terms of its stacking sequence and bilayers, b) 6H-SiC in terms of its stacking sequence and bilayers. Figure was taken from reference [www1].

1.1.2 RADIATION DAMAGE

1.1.2.1 DAMAGE ACCUMULATION

Bombarding a SiC crystal with energetic ions induces damage which distorts the crystalline structure. This irradiation-induced damage inside the SiC increases with increasing fluence, until a certain fluence level is reached, where the crystalline SiC collapses into an amorphous band at the depth of maximum radiation damage density.

A further increase in the ion fluence, after the initial collapse, will lead into a widening of the amorphous band until the damage covers the entire irradiated area. In this case the region of ion irradiation becomes amorphous. There has been a long standing debate regarding the atomic kinetics of the crystalline-amorphous transition. In general, amorphisation in SiC occurs in two ways; homogenously, or heterogeneously [Web00]. Homogenous amorphisation is associated with a progressive process due to accumulation of point defects, or a specific point defect. During this process the defects accumulate, until a certain defect density level is reached, at which point the SiC spontaneously undergoes the crystalline-to-amorphous transition. This kind of amorphisation process is usually associated with electron irradiation, and low mass ions. The heterogeneous amorphisation process is associated with several possible mechanisms for the crystalline-to-amorphous transition in SiC. These include: Direct impact amorphisation; the local accumulation of high density defects due to collision cascade overlaps; the nucleation and growth mechanism; a combination of more than one mechanism. The Hecking model, [Hec86], is an example of a combination of two mechanisms, the direct impact amorphisation and stimulated amorphisation at the amorphous-crystalline interface.

An increase in temperature during ion implantation into crystalline SiC can cause a mitigation of the amorphous process by decreasing the defect density, and ultimately the fraction of the amorphous component inside the SiC. This effect of temperature on the amorphisation process can be attributed to simultaneous recovery processes which occur by the enhancement of the defect migration and recombination in the crystalline structure, ion-defect diffusion in the amorphous state, epitaxial growth at the crystalline amorphous interface. Several models have be proposed to elaborate on these recovery process [Mor70][Web94a][Web94b]. Weber et al, [Web98], applied the models described by Morehead et al., [Mor70], and Weber et al., [Web94a], and determined activation energy for the recovery processes after irradiating with electrons and various ions. The obtained activation energies were consistent with irradiation induced recovery process in the temperatures below 500K. The models were also used to determine the critical temperatures for the various ions and electron irradiation. The results thus obtained showed that there is an increase in amorphisation dose and a decrease in critical temperature with decreasing mass. These results were similar to those obtained by Snead et al. [Sne99]. E. Wendler et al., [Wen98],

summarized in a table the results showing the critical values of displacements per atom and energy deposition per atom, which are necessary for amorphisation of SiC for several irradiation ions and temperatures. These results suggest that there must be an increased efficiency in the recovery processes with decreasing mass. The increase in efficiency in the recovery process can be attributed to the increased production of isolated Frenkel pairs, low energy cascades and lower probability of anti-site production which may be required for amorphisation in SiC [Hob97] or the increase in electronic to nuclear stopping which might lead to ionisation induced recovery processes. Weber et al, [Web12], further examined their data by applying a dynamic model in order to determine the nature of the recovery processes. Their results showed that the behaviour, increased efficiency in the recovery processes with decreasing mass, was consistent with irradiation-enhanced recovery processes. However, ionisation induced recovery played a significant role only in the electron irradiation case, as for the ion mass dependence, the ionisation induced recovery was not too significant. These results were consistent with the model proposed by [Web00], which stipulates that when the critical temperature for amorphisation depends on ion mass, the dominant recovery process must be irradiation-enhanced.

The damage retained after high temperature implantation is different from that retained after room temperature implantation. Several studies have been done to investigate this discrepancy [Hef95][Hef96][Wes95][Wen98]. Implantation at room temperature at low fluences, and implantation at elevated temperatures at higher fluences, introduces comparable damage into the SiC crystal. The SiC does not collapse into an amorphous state rather it preserves some damage in its crystalline structure. Despite the fact that both cases do not amorphise the SiC, the damage retained in each instance is different. Implantation at room temperature, at low doses produces a defect profile that is comparable to the distribution of the ions inside the SiC. However, implantation at elevated temperatures and high dose, causes a shift in the damage profile to deeper depths, thus the damage distribution is different to the distribution of the implanted ions. Consequently, the defect morphology under the different irradiation condition is considered as different due the diffusion, recombination and transformation of defects as a consequence of the high temperature during implantation [Hef95][Wes95][Wen98]. This discrepancy in defect morphology is directly evident in the annealing behaviour of the differently irradiated SiC samples.

1.1.3 RADIATION DAMAGE ANNEALING

As noted in the previous section irradiation of the crystalline SiC results in either an amorphous or non-amorphous structure depending on the irradiation details. As a consequence, the annealing dynamics of amorphous and non-amorphous SiC is different.

1.1.3.1 AMORPHOUS LAYER ANNEALING

When ion implantation results in an amorphous layer the annealing of the damage is quite difficult. The damage does not completely anneal out up until temperatures near and above 1500 ^{o}C [Boh87][McH93][Wes95][Hef96][Wen98]. Annealing an amorphous SiC at temperatures below 700 ^{o}C leads to the relaxation of the metastable amorphous SiC structure and increases the density of the SiC, through point defect recombination [Hof99]. It is only after annealing at temperatures near and above 1000 ^{o}C that re-crystallisation of the SiC is significant enough for observation [Hof99][Aud07][Wen98][Pac96a][Pac96b]. Further annealing the amorphous SiC at temperatures above 1000 ^{o}C but below 1500 ^{o}C only results in slight reduction of the amorphous layer from the amorphous crystalline interface [Boh87][Hla12][Wes95]. Many authors have shown that annealing SiC above 1000 ^{o}C already forms polycrystalline grains in the previously amorphous region [Pac96a][Wen98][Hla12]. It is only after annealing at temperatures near and above 1500 ^{o}C that the SiC retains its monocrystalline structure, although highly defective.

1.1.3.2 NON-AMORPHOUS LAYER ANNEALING

The annealing of non-amorphous layers is somewhat different to that of an amorphous layer. A non-amorphous layer can be obtained in two ways: Through low dose implantation and low temperature; alternatively, the same effect of a non-amorphous layer can be achieved through high temperature implantation. Although the damage produced by the latter methods can be viewed as comparable, i.e. both are non-amorphous; the annealing dynamics are certainly different. In the instance of low

temperature and low dose implantation the SiC re-crystallises almost completely by 1200 ^{o}C. However, for the comparable damage retained after higher temperature implantation the SiC does not re-crystallise to the same extent after annealing at 1200 ^{o}C, temperatures above this are required. This can be attributed to the damage morphology difference in the two cases. The damage in the low temperature and low dose case constitutes mainly of point defects and point defect clusters, whereas in the high temperature and high dose case the damage is characterised by more complex and thermally stable defects. The point defects and point defect clusters anneal out monotonically with increasing temperature until they recombine completely at temperatures around 1200 ^{o}C [McH93][Boh87][Wen98][Pac96][Cal97]. Complex and thermally stable defects form during the in-situ annealing at the implanter, this implies that as already mentioned, the high temperature implantation causes diffusion; recombination and transformation of defects. One may also argue that the reason for the annealing hardness of the high temperature and high dose implantation is related to the increased concentration of impurities inside the SiC sample thus restraining the annealing of the defects.

1.1.4 DIFFUSION BEHAVIOUR

A number of studies have been done on the diffusion of other fission products in SiC. These would include but are not limited to the diffusion of xenon [Fuk76], cesium [Aud07], silver [Hla10], and iodine [Fri10]. However, there has not been much progress as far as the diffusion of Kr in 6H-SiC is concerned. This project aims to bridge this knowledge gap and investigate the diffusion behaviour of Kr in 6H-SiC. This was done by implanting 360 keV Kr ions to a fluence of 2×10^{16} ions/cm^2 into 6H-SiC at three different temperatures, i.e. room temperature, 350 ^{o}C and 600 ^{o}C. The investigation was conducted by using the Rutherford backscattering technique (RBS) in order to assess the diffusion. Since implanting at different temperatures has been shown to result in different orders of retained radiation damage, RBS in the channelling mode (RBS-C) was used to assess the amount of radiation damage retained after each implantation. Further, annealing experiments, in the temperature range 1000 – 1500 ^{o}C, were performed to determine the influence of temperature on the diffusion of the implanted Kr in the SiC. Subsequently, the recovery of the

retained damage after implantation, and its influence on the diffusion, was also investigated as a function of annealing temperature.

The rest of this dissertation is arranged as follows: In chapter 2 a brief discussion of the diffusion theory is given; Chapter 3 gives a discussion of ion implantation and pertinent processes; Chapter 4 discusses the analytical techniques that were used in this project; In chapter 5 the experimental method followed in completing this project is explained; Chapter 6 discusses the findings of this project; Chapter 7 gives the summary and conclusions based on the entire findings of this project.

1.2 REFERENCES

[Aud07] A. Audren, A. Benyagoub, L. Thomè, F. Garrido, Nucl. Instr. and Meth. **B 257** (2007) 227.

[Boh87] H.G Bohn, J.M Williams, G.M Begun, J. Mat. Res. **2** (1987) 107.

[Cal97] L. Calcagno, M.G. Grimaldi, P. Musumeci, J. Mat. Res. **12** (1997) 1727.

[Fri10] E. Friedland, N.G. van der Berg, J.B. Malherbe, R.J. Kuhudzai, A.J. Botha, E. Wendler, W. Wesch, Nucl. Instr. and Meth. **268** (2010) 2892.

[Fuk76] K. Fukuda, K. Iwamoto, J. Mat. Sci. **11** (1976) 522

[Hec86] N. Hecking, K.F. Heidemann and E. Te Kaat, Nucl. Instr. and Meth. **B 15** (1986) 760.

[Hef95] A. Heft, E. Wendler, T. Bachmann, E. Glaser, W. Wesch, Mat. Sci. Eng. **B 29** (1995) 142.

[Hef96] A. Heft, E. Wendler, J. Heindl, T. Bachmann, E. Glaser, H.P Strunk, W. Wesch, Nucl. Instr. and Meth. **B 116** (1996) 239.

[Hla10] T.T. Hlatshwayo, (2010). "Diffusion of Silver in 6H-SiC", PhD Thesis, University of Pretoria, Physics department.

[Hla12] T.T. Hlatshwayo, J.B Malherbe, N.G. van der Berg, L.C. Prinsloo, A.J. Botha, E. Wendler, Nucl. Istr. and Meth. **B 274** (2012) 120.

[Hob97] L.W. Hobbs, A.N. Sreeram, C.E. Jesurum, B.A. Berger, Nucl. Inst.and Meth. **B 116** (1997) 18.

[Höf99] A. Höfgen, V. Heera, F. Eichhorn, W. Skorupa, W. Möller, Mat. Sci. Eng. **B 61-62** (1999) 353.

[McH93] C.J. Mchargue, J.M. Williams, Nucl. Instr. and Meth. **B 80/81** (1993) 889.

[Mor70] F.F. Morehead, B.L. Crowder, Rad. Eff. **6** (1970) 27.

[Nic02] H. Nickel, H. Nabiekel, G. Pott, A.W. Mehner, Nucl. Eng. and Des. **217** (2002) 141.

[Pac96a] Y. Pacaud, W. Skorupa, J. Stoemenos, Nucl. Instr. and Meth. **B 120** (1996) 181.

[Pac96b] Y. Pacaud, J. Stoemenos, G. Brauer, R.A Yankov, V. Heera, M. Voelskow, R. Kögler, R. Skorupa, Nucl. Instr. and Meth. **B 120** (1996) 177.

[Sne99] L.L. Snead, J.C Hay, J. Nucl. Mat. **273** (1999) 213.

[Web00] W. J Weber, Nucl. Instr. and Meth. **B 166/167** (2000) 98.

[Web12] W.J Weber, Y. Zhang, L. Wang, Nucl. Instr. and Meth. **B 277** (2012) 1.

[Web94a]W.J. Weber, R.C. Ewing, L.M. Wang, J. Mat. Res. **9** (1994) 688.

[Web94b]W.J. Weber, L.M. Wang, Nucl. Instr. and Meth. **B 91** (1994) 63.

[Web98] W.J. Weber, L.M. Wang, N. Yu, N.J. Hess, Mat. Sci. Eng. **A 253** (1998) 62.

[Wen98] E. Wendler, A. Heft, W. Wesch, (1998). Nucl. Instr. and Meth. **B 141** (1998) 105.

[Wes95] W. Wesch, A. Heft, E. Wendler, T. Bachmann, E. Glaser, Nucl. Instr. and Meth. **B 96** (1995) 335.

[Wes96] W. Wesch, Nucl. Instr. and Meth. **B 116** (1996) 305.

[www1] *www.grc.nasa.gov/WWW/**SiC**/publications/CRCChapter2ndEd.pdf* - 2014/03/04.

[Zho11] X.W. Zhou and C.H. Tang, Prog in Nucl. Ener. **53** (2011) 182.

[Zol05] Z. Zolnai, (2005). PhD Thesis, Department of atomic Physics, Budapest university of Technology and Economics.

CHAPTER 2 DIFFUSION

Atoms in a solid material are always oscillating about their equilibrium position within the crystal, with a Maxwell-Boltzmann energy distribution. If the temperature increases, the thermal energy of the atoms increases causing atomic vibrations in the crystal to intensify. The atoms in a crystal can change lattice sites if they have enough energy to overcome the potential energy barrier between their neighbours. A large part of this energy involves breaking the bonds between neighbouring atoms, and the strain energy required to displace the neighbouring atoms so as to create adequate space for the atom to move. High temperature gas-cooled reactors (HTGR) operate at high temperatures. Consequently the atoms in a crystal will have high energies. Therefore in such conditions can overcome the potential barrier between their neighbours and leave their lattice sites.

Once an atom leaves its lattice site it can collide with other atoms in the crystal and, although unlikely, displace them if the atom has sufficient energy. In an inhomogeneous material a net drift of atoms is against a concentration gradient. The atoms tend to move from a region of high concentration to a region of low concentration in order to minimize the free energy of the system. In homogenous materials atoms are also capable of traversing the crystal, however for this type of material there is no preferred direction. Whether or not there is a preferred direction, the motion of atoms from one lattice position to another one is known as diffusion. It is a type of transport mechanism by which atoms in a crystal move.

2.1 DIFFUSION MECHANISMS

Although there may be instances when the presence of defects can hinder diffusion, it is however in most cases enhanced by the presence of these imperfections in the crystal. These imperfections include point defects, linear and surface defects. Diffusion is generally faster along linear and surface defects at low temperature. Lattice diffusion normally takes place through the movement of point defects. This is excluding instances like ring and exchange mechanisms of diffusion, which are

improbable in cases of highly close packed crystals. In a crystal, defects are inevitable, they can be found both on the surface of a crystal and within the crystal itself. Even under controlled crystal growth processes defects are always found in crystals, they can also be introduced during ion implantation and irradiation. In this project Kr was implanted into 6H-SiC and ultimately annealed at high temperatures, thus knowledge of the defects and their link to diffusion is important in the analysis of the results. As a consequence this section discusses defect dominated diffusion mechanisms.

2.1.1 VACANCY MECHANISM

A vacancy is a point defect which constitutes an unoccupied lattice site. Vacancy diffusion occurs when an atom jumps from its lattice position to occupy the vacant position. The vacancy itself is seen to be moving since the site which was occupied by the atom remains unoccupied. Figure 2.1 shows the schematic illustration of this diffusion mechanism. The vacancy mechanism depends on several factors. This diffusion mechanism will be favoured provided the diffusing atom is adjacent to the vacancy. Also, diffusion by this mechanism depends on the availability of these defects which is given by:

$$N_{vf} = N \exp(-\frac{E_{vf}}{k_B T}) \tag{2.1}$$

N is the total number of atomic sites, N_{vf} is the number of vacancies per unit volume and, E_{vf} is the energy required for the formation of vacancies, k_B is the Boltzmann constant and T denotes the absolute temperature in Kelvins. From equation (2.1) it can be seen that the number of vacancies increases with increasing temperature. At very high temperatures, close to the melting point of solid diffusion can occur via bound pairs of vacancies. These are called divacancies [Hei04]. Frequently, during the diffusion process vacancies may also agglomerate to form more complex clusters in order reduce the strain in the surrounding crystalline lattice.

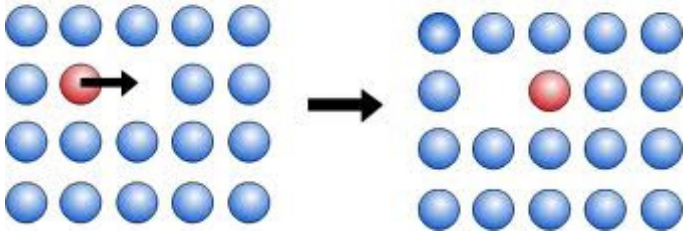

Figure 2.1: Schematic illustration of vacancy diffusion in a crystal. The red circle represents the atom that will move to fill the empty space, i.e. the vacancy. Figure taken from reference [www1]

2.1.2 INTERSTITIAL MECHANISM

An interstitial site is the space between any four atoms in a 2D crystal lattice. An interstitial atom is one which occupies an interstitial site. Interstitial diffusion occurs when an interstitial atom jumps from one interstitial site to another interstitial site. Figure 2.2 shows an illustration of this diffusion mechanism. The interstitial mechanism is preferred in the case of atoms with a smaller radius than the host atoms. This is because larger atoms would require a significant amount of energy to pass through the barrier separating the interstitials. However, it is generally faster than vacancy diffusion since in a given crystal there are more interstitials than vacancies.

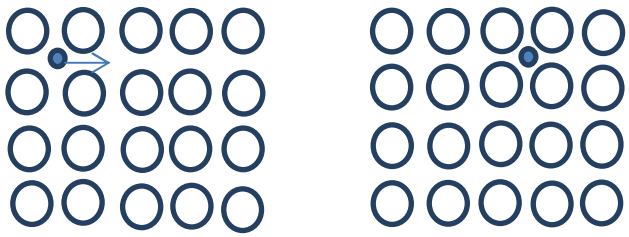

(a) (b)

Figure 2.2: Schematic illustration of interstitial diffusion. (a) Depicts the state of the crystal before diffusion, and (b) gives the state of the crystal after diffusion.

2.1.3 INTERSTITIALCY MECHANISM

In the case when the interstitial mechanism becomes improbable for an interstitial atom, the atom may move by another mechanism. In the interstitialcy mechanism an interstitial atom pushes one of its nearest neighbours on a normal lattice position to an interstitial position, and itself occupies the lattice site of the displaced atom. Figure 2.3 illustrates this mechanism. There are two types of movements that can occur via the interstitialcy mechanism. If the atom is pushed in the same direction as the motion of the interstitial atom, the movement is said to be collinear, as shown in figure 2.3(a). When the atom is pushed in a direction non-linear to the direction of the motion of the interstitial atom the movement is said to be non-collinear, as shown in figure 2.3(b). This mechanism of diffusion is important for radiation induced diffusion since then vacancies and interstitials are created in equal amounts by irradiation of crystals with energetic particles [Hei05].

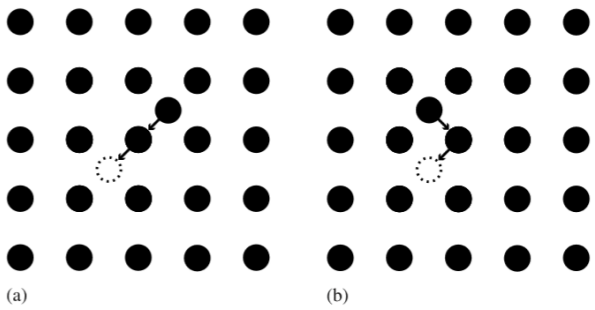

Figure 2.3: Schematic illustration of interstitialcy diffusion. (a) Depicts the collinear interstitialcy diffusion, and (b) gives the non-collinear interstitialcy diffusion. Taken from reference [Was07].

2.2 FICK' S LAWS OF DIFFUSION

Now that the mechanisms by which atomic diffusion occurs have been discussed, we continue the discussion of diffusion by looking at the rate at which atoms diffuse. This information can be obtained from Fick's laws of diffusion. Fick's first law gives the

mathematical formulation for the case where the atoms flow down a concentration. This law is given in one dimension as:

$$J = -D\frac{dC}{dx} \tag{2.2}$$

J is the flux of the atoms through a unit area per unit time, C is the concentration of the atoms, dC/dx is the concentration gradient, and the minus sign denotes that the flow of particles is from a region of high concentration to a region of low concentration. Essentially, Fick's first law gives the relationship between the number atoms crossing a unit area per unit time and the change in the concentration of atoms per unit length at some position x.

For most practical situations the concentration of particles within a certain region changes with time, as a consequence the concentration gradient also changes. Figure 2.4 illustrates this situation. Looking at the figure let's consider a region dx enclosed between two planes, with particle flux through plane1 as j_1 and particle flux through plane2 as j_2. The concentration in dx increases with time when j_1 is greater than j_2. To conserve matter we require that the relationship between the change in concentration per unit time and the gradient of the flux be given as:

$$\frac{\partial C}{\partial t} = -\frac{\partial J}{\partial x} \tag{2.3}$$

Although the concentration changes with time and the flux changes with position, at any given point and time equation (2.3) still holds:

$$\frac{\partial C}{\partial t} = -\frac{\partial}{\partial x}(-D\frac{\partial C}{\partial x}) \tag{2.4}$$

If we consider D to be a constant with respect to changing position, then:

$$\frac{\partial C}{\partial t} = D\frac{\partial^2 C}{\partial x^2} \tag{2.5}$$

The results contained in equations (2.4) and (2.5) allow us to study diffusion in the non-steady state and these equations are well known as Fick's second law.

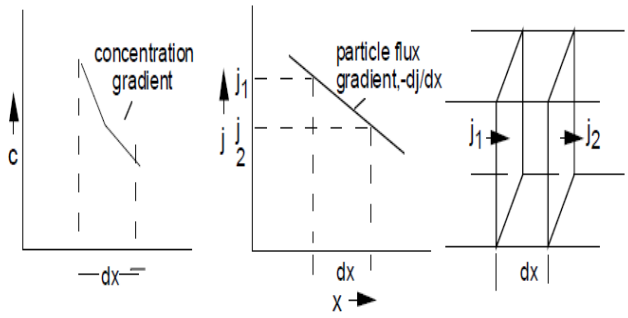

Figure 2.4: schematic illustration of Fick's second law. The picture on the left shows how the concentration gradient changes with time, the middles picture shows how the flux changes with position, and on the right is the schematic of the region, dx, through which the particles pass. Figure taken from reference [www2].

2.3 THE DIFFUSION COEFFICIENT

In this study, the diffusion of Kr in 6H-SiC was investigated using the RBS technique discussed in chapter 4, RBS is based on the analysis of the energy of backscattered charged particles. By comparing the as-implanted Kr depth profile and post-annealing Kr depth profiles the diffusion coefficient can be extracted. This method of extracting diffusion coefficient is only applicable in Gaussian profiles. If the as implanted depth profile is Gaussian; Fick's diffusion equation, equation (2.5), for the dilute limit leads to concentration profiles after annealing for a time t that can be expressed as the Gaussian function [She94]:

$$C(x,t) = K[\pi Dt]^{-\frac{1}{2}} \exp\left(-\frac{x^2}{4Dt}\right) \qquad (2.6)$$

where K is an adjustable constant, while the position of maximum concentration is unchanged at $x=0$. If the full width at half maximum (FWHM) after annealing for a

time t is defined as $W(t)$, then the relationship between the post-annealing width at time t – and the width of the as-implanted depth profile is given by:

$$[W(t)]^2 = 4Dtln(2) + [W(0)]^2 \tag{2.7}$$

From equation (2.7), the diffusion coefficient can be determined from the slope of $W(t)^2$ versus annealing time t.

Diffusion coefficients in solids generally have a significant dependence on temperature. The empirically determined relationship between temperature and the diffusion coefficient is given by the Arrhenius relation:

$$D = D_0 \exp(-\frac{E_a}{k_B T}) \tag{2.8}$$

In equation (2.8) D_0 is the pre-exponential factor, E_a is the activation energy for diffusion, k_B is the Boltzmann constant and T denotes the absolute temperature in Kelvins.

The diffusion co-efficient was, however, not calculated for this project since the isothermal annealing experiments were not performed.

2.4 GRAIN BOUNDARY DIFFUSION

The section on diffusion mechanisms only considers cases of diffusion through point defects. However, since a crystal can have other types of defects it makes sense to also consider how these could influence the movement of atoms in a crystal. Grain boundaries are interfacial defects separating two grains or crystals having different crystallographic orientations. They can be seen as a two-dimensional transition region between two grains. Within this region which is a few atomic distances wide there is a mismatch from the crystalline orientation of one grain to that of an adjacent one.

Atoms are bound less regularly along a grain boundary; as a consequence the atoms in a grain boundary are at a higher energy state than atoms in a normal lattice position [Cal07]. This additional energy allows for diffusion in the boundary to be faster than in the lattice [Gup04], as a result grain boundaries are known as high diffusivity paths. For a detailed discussion on grain boundaries and high diffusivity paths, the books by [Hei04][Gup04] should be consulted.

2.5 REFERENCES

[Cal07] W.D. Callister, (2007). "Materials Science and Engineering an Introduction", John Wiley and Sons, USA.

[Gup04] D. Gupta, (2004). "Diffusion processes in advanced technological material", Yorktown Height, New York.

[Hei04] P. Heitjans, J. Karger, (2005). "Diffusion in Condensed Matter", Springer, Netherlands.

[She89] P. Shewmon, (1989). "Diffusion in solids". 2nd ed., TMS,USA.

[Was07] G.Was, (2007). "Fundamental of Radiation Materials Science", Springer-Verlag Berlin Heidelberg.

[www1] www.doitpoms.ac.uk/tlplib/diffusion/diffusion_mechanism.php , 10/11/11.

[www2]www.uio.no/studier/emner/matnat/kjemi/KJM5120/v05/undervisningsmateriale/KJM5120-Ch5-Diffusion.pdf - 26/05/14.

CHAPTER 3 ION IMPLANTATION

Energetic particles which are bombarded onto a target surface will interact with the surface atoms. The surface interaction will result in some of the particles being backscattered off the surface while the rest will penetrate into the sample. The fate of those particles which penetrate into the sample will largely depend on the processes which control their energy loss. This is because they will undergo a series of collision or interactions with the target atoms and/or target electrons. Each collision results in a transfer of energy from the projectile ion to the target atom or target electrons. While some ions, will after penetration, still exit the sample through backscattering events, a certain fraction will eventually be imbedded inside the sample as a consequence of the energy loss. The process which involves energetic ions penetrating a target material and ultimately coming to rest inside the material is known as ion implantation.

3.1 ENERGY LOSS PROCESSES

As an ion enters the material it, slows down, and its kinetic energy diminishes. The energy, ΔE, that the projectile ion loses as it travels a distance, Δx, depends on a few factors: These include the identity and velocity of the projectile; also important are the density and composition of the target material. The ratio of the energy loss ΔE to the distance traversed by the ion inside the material Δx is defined as the specific energy loss:

$$\lim_{\Delta x \to 0} \frac{\Delta E}{\Delta x} = \frac{dE}{dx} \tag{3.1}$$

The stopping cross-section of a material is defined by taking the ratio of the energy loss to the atomic density of the material N, and it is referred to for the most parts of this section as the stopping power of the material:

$$S = \frac{1}{N}\frac{dE}{dx} \tag{3.2a}$$

Energy loss in materials does not occur via a single process. In this discussion we will distinguish between two of the fundamental processes of energy loss: nuclear and electronic energy loss. Nuclear energy loss is due to elastic screened Coulomb collisions between the nuclei of the projectile ion and the target atom, and electronic energy loss is due to the inelastic (elastic) collisions of the projectile with the bound (free) electrons of the target atoms. The nuclear energy loss and electronic energy loss are treated as acting independently. As a result of the independence of the nuclear and electronic stopping, the total stopping power is given as a mere sum:

$$S = \left(\frac{1}{N}\frac{dE}{dx}\right)_n + \left(\frac{1}{N}\frac{dE}{dx}\right)_e \qquad (3.2b)$$

The subscripts n and e denote the nuclear and electronic stopping powers, respectively – Please note that the e in the above formulae has a different meaning from the e which will be used to represent the electronic charge. The variation of the stopping powers with ion velocity is shown in the schematic of figure 3.1, below. As can be seen from figure 3.1 nuclear stopping tends to dominate at low ion velocities. At high ion velocities electronic stopping takes over as electronic collisions become important.

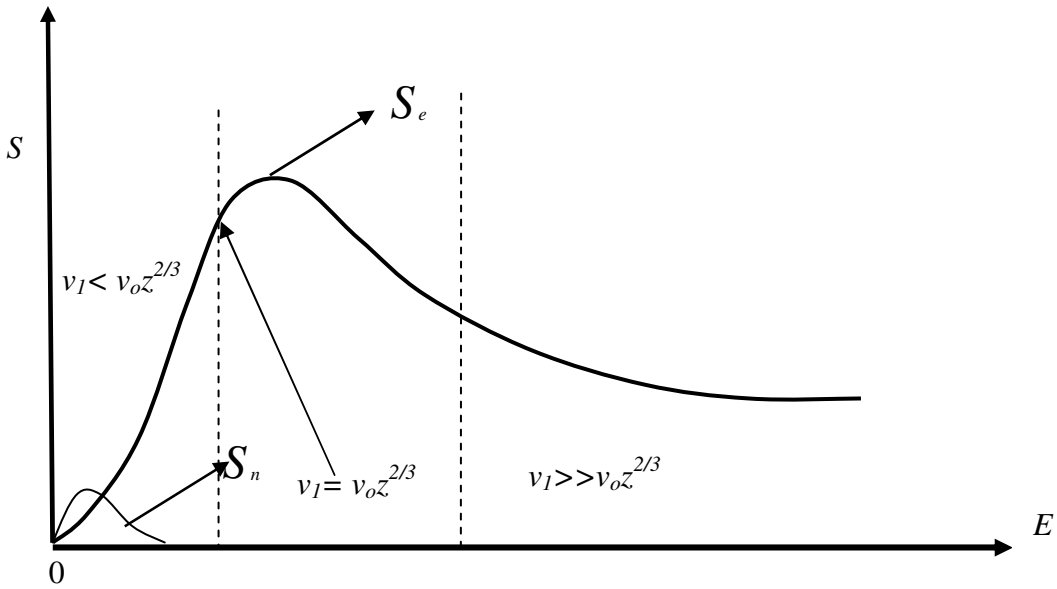

Figure 3.1: The variation of the nuclear stopping power and the electronic stopping power as a function of projectile energy.

3.1.1 NUCLEAR ENERGY LOSS

Nuclear energy loss is due to a collision between a projectile ion and a screened target nucleus. The nuclear energy loss is formulated by treating the interaction of the projectile and the target nucleus as an elastic two body collision. It dominates at low ion velocities as can be seen from figure 3.1. Nevertheless, the ions are considered to have energies above 10 eV, which is the approximate energy needed for an atom to be displaced from its lattice position. The ion energies of consideration in this section, also, do not lead to inelastic nuclear excitations, i.e. nuclear reactions or Coulomb excitation.

To setup the expression for the energy transferred to a target atom by the projectile ion, the kinematics of a two-body scattering collision has to be reviewed. Although the interaction between the two particles can be likened to a collision of two billiard balls, this case in particular however, has to take into consideration the electrostatic nature of the two particle interaction. The interaction between the particles can be modelled by defining an interaction potential. The computation of the nuclear stopping is further complicated by the fact that there is no single interatomic potential which can be used to describe the interaction between any two particles – The potential of choice depends on the conditions of the collision. In references [Zie85] and [Was07] a somewhat detailed description of the probable potentials is given. An important point which is emphasised in [Was07] is that the type of interatomic potential which is relevant to any particular situation will most likely depend on the particle energies, hence the distance of closest approach between the particles. For the purposes of modelling the interaction between the projectile ion and the target atom we adopt the interatomic potential of the type:

$$V(r) = \frac{Z_1 Z_2 e^2}{r} f(Z_1, Z_2, r) \tag{3.3}$$

where in the above equation Z_1 and Z_2 are the atomic numbers of the ion and target atom, respectively, $f(Z_1,Z_2,r)$ is a screening function which depends on the model used for the particular ion-atom interaction. Figure 3.2, shows the schematic presentation of the interaction between the two particles. As the projectile ion approaches the

target atom, the target atom recoils through an angle α and the projectile itself is pushed off due to the interaction potential through an angle θ. These are the directions of recoil and scattering in the laboratory frame of reference, respectively. However, the problem is solved in the centre of mass reference frame due to simplifications inherent in this frame of reference [Zie85][www2]. For example the relative motion of the two particles can be treated as that of a single particle in a central potential. The energy transferred during a two-body scattering collision of the projectile ion and the target atom can be described as a function of the projectile's incident energy, E_0, and its impact parameter, b. The impact parameter is defined as the perpendicular distance between the initial path (prior to scattering) of the projectile and the centre of the atom that the projectile is approaching. The energy transferred to the target atom is determined from the conservation of energy and momentum to be:

$$T = \frac{4M_1M_2}{(M_1+M_2)} E_0 \sin^2(\frac{\Theta}{2}) \tag{3.4a}$$

$$\Theta = \pi - 2\alpha \tag{3.4b}$$

where Θ is the projectile ion's scattering angle in the centre of mass system (not shown in figure 3.2), M_1 is the mass of the projectile ion, M_2 is the mass of the target atom.

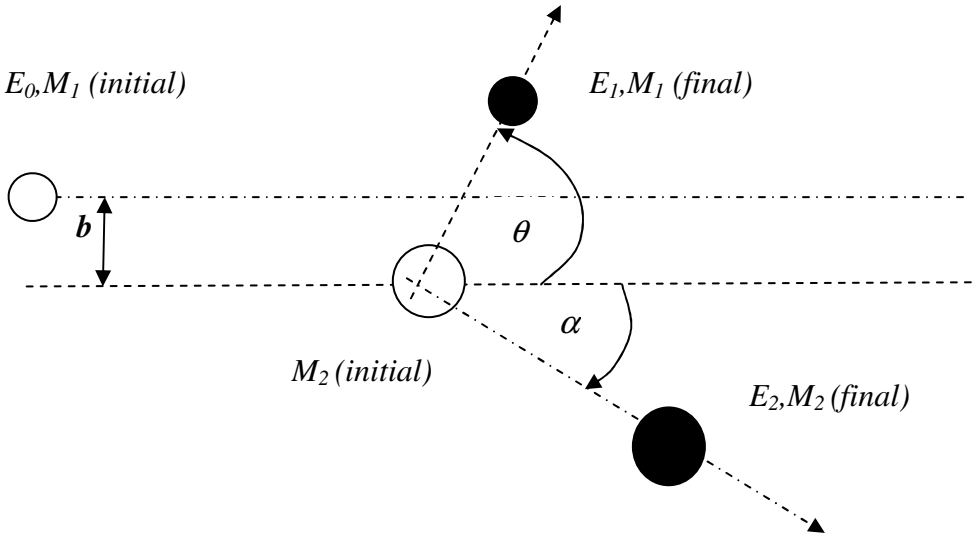

Figure 3.2: A schematic presentation of the interaction of the projectile ion and a target atom.

From figure 3.2 it is can be seen that the energy, E_2, of the target atom after it recoils is equal to the energy transferred, T, calculated above in equation (3.4a). The discussion of energy loss up to this point has been focused purely on single atomic encounters between isolated particles. However, during ion implantation an ion undergoes a series of such encounters with the lattice atoms of a solid. It, therefore, follows that on average ions will lose a certain amount of energy per unit distance travelled inside the solid, $(dE/dx)_n$, as a consequence of these individual elastic nuclear encounters. By definition the mean energy loss or transfer in a single collision is given by:

$$\overline{T} = \frac{\int_0^\infty T \cdot d\sigma}{\int_0^\infty d\sigma} \tag{3.5a}$$

In the case where there are N target atoms per unit volume, then the mean energy loss per unit distance travelled becomes:

$$\frac{dE}{dx_n} = N \cdot \bar{T} \int_0^\infty d\sigma = N \int_0^\infty T d\sigma \tag{3.5b}$$

In the above equations, $d\sigma = 2\pi b db$, is the differential collision cross-section. The nuclear stopping cross-section can also be obtained from the above equations according to equation (3.2b):

$$S_n = \int_0^\infty T \cdot 2\pi b db = 8\pi E_0 \frac{M_1 M_2}{(M_1 + M_2)^2} \int_0^\infty \sin^2(\frac{\Theta}{2}) b db \tag{3.5c}$$

$$S_n = Q \int_0^{b_{\max}} \sin^2(\frac{\Theta}{2}) b' db' \tag{3.5d}$$

$$Q = \frac{8\pi M_1 M_2}{(M_1 + M_2)^2} E_0 \tag{3.5e}$$

The above treatments of nuclear energy loss are performed under the crucial assumption that each nucleus acts independently of every other nucleus. In equation (3.5d) the variables *b'* and *db'* are used as dummy variables to avoid confusion with the integration limit. Also, in equation (3.5d) b_{max} is the maximum possible impact parameter which will result in energy transfer from the projectile ion to the target atom. Since real potentials are generally infinite, the impact parameter is also taken as infinite. To overcome this hurdle the hard-sphere approximation is generally used for low energy collisions. A detailed discussion of the hard-sphere approximation and real potentials can be obtained in references, [Was07] and [Car76].

3.1.2 ELECTRONIC ENERGY LOSS

Electronic stopping is due to electronic collisions, where the projectile ion interacts with the substrate electrons leading to their possible excitation and emission [Lin65]. The projectile loses energy inelastically when it interacts with core electrons, however if it interacts with free electrons in metals the energy loss can be approximated as elastic.

There is no single model that is used to describe the electronic energy loss. When the ion has a low velocity it will hold on to most of its electrons and this to some extent will screen the field of the projectile. When the projectile, however, moves at velocities higher than its most tightly bound electrons, it will tend to be stripped off its electrons – And this particular instance is treated using a quantum mechanical perturbation treatment [Lin53][Boh48][Bet30][Blo33]. The treatment of these two cases is different. Most of the theoretical work done on electronic stopping is based on the Thomas-Fermi statistical model. As a consequence the Thomas-Fermi velocity, $v_{TF} = v_0 Z_1^{2/3}$, is used as a reference velocity with the Bohr velocity v_0 given by $v_0 = Ke^2/\hbar = 2.2\times10^6\ m.s^{-1}$. K, is the Coulomb constant which has a numeric value of $9\times9^{10} N.m^2/C^2$. In the case of Kr ions implanted into 6H-SiC, $v_{TF} = 2.4\times10^7\ m.s^{-1}$, and the incident velocity of the 360 keV Kr ions was $v_1 = 9.1\times10^5\ m.s^{-1}$.

In the high velocity region (also known as the Bethe-Bloch region), the projectile particle has velocity, $v_1 >> v_{TF}$. The particle moves faster than its ground state electrons. The collision between the projectile and the target electrons may be described by a classical impact parameter b and a collision time $\tau = b/v_1$. Distant collisions which correspond to a large impact parameter and ultimately a longer collision time are negligible and considered as adiabatic since a negligible amount of energy is transferred. However, for the close impact collisions the electrons will recoil more strongly, the binding and mutual interaction of the electrons can be ignored, and a significant amount of energy is transferred. Under these classical conditions Bohr was able to formulate the electronic stopping power for high velocity projectiles [Boh13][Zie99]:

$$S_e = \frac{4\pi Z_1^{\,2} e^4}{M_1 v_1^{\,2}} B \qquad (3.6a)$$

It was not until Bethe united the classical model by Bohr with quantum mechanics that the appropriate expression for the "atomic stopping number" B was established [Bet30]:

$$S_e = \frac{4\pi Z_1^2 e^4}{M_1 v_1^2} Z_2 \ln\left(\frac{2M_1 v_1^2}{I}\right) \tag{3.6b}$$

$$B = Z_2 \ln\left(\frac{2M_1 v_1^2}{I}\right) \tag{3.6c}$$

In the above formulation I is the average electron excitation potential [Blo33]. $I = kZ_2$, where k lies between 9.5 and 11 eV. Additionally, we note that in this region the stopping power decreases with increasing energy. A high kinetic energy implies a high ion velocity this consequently leads to a reduced interaction time between the projectile and the target electrons.

For projectiles with $v_1 < v_{TF}$, the Bethe-Bloch formulation no longer applies. There is a high probability that the projectile is not fully ionised and the target atom ground state electrons are no longer involved in the stopping process. There are two competing models for the stopping cross-section in this velocity range, viz. the Firsov and the Lindhard-Scharff models [Fir59][Lin61a][Lin61b][Lin65][Zie85]. The models are completely different and yet they converge to the same result - the stopping power is directly proportional to the velocity of the projectile, at least approximately so. The Firsov model is based on a quasi-molecule, which is a geometrical model of momentum exchange between the projectile and the target atom through electron transfer. The Lindhard-Scharff model is based on the electron gas model and the Thomas-Fermi atomic model. The electronic stopping as derived by Lindhard and Scharff is given by:

$$S_e = \zeta_e 8\pi N a_0 Z_1 Z_2 (Z_1^{2/3} + Z_2^{2/3})^{-3/2} \cdot \frac{v_1}{v_0} \tag{3.7}$$

where ζ_e is a dimensionless constant of the order $Z_1^{1/6}$ – This term is added as a fitting parameter, a_0 is the Bohr radius. As can been noted from the above equation, the electronic stopping is proportional to the projectile velocity contrary to the case where the Bethe-Bloch formalism holds.

The intermediate velocity region then becomes $v_L < v_1 < v_h$, where v_L and v_h corresponds to the velocity in the low and high energy regions, respectively – figure 3.1. There are no adequate theoretical treatments for this region only semi-empirical treatments exist. At these velocities the projectile might capture electrons from the target atoms, thus altering its charge state. This velocity region is often treated as the low-velocity limit to the Bethe-Bloch region. Thus, the same formulation of Bethe-Bloch is applied only now instead of the actual charge Z_1 an effective charge is used [Zie85][Zie99]:

$$\frac{Z_1^*}{Z_1} = 1 - \exp\left(\frac{-v_1}{v_0 Z_1^{2/3}}\right) \tag{3.8}$$

where Z_1^* is the statistical net charge – Defined as the charge state required to reduce the Bethe-Bloch stopping to agree with experimental stopping values.

3.2 STOPPING POWER IN COMPOUNDS

The stopping power of a compound may be estimated as a linear combination of the individual stopping powers of the constituent elements. This estimation may be made under the assumption that the interaction between the ion and target atom is independent of the surrounding target atoms, and it is known as Bragg's rule. For a compound A_mC_n, Bragg's rule, for the stopping power is given by [Bra05]:

$$S^{AC} = mS^{A} + nS^{C} \tag{3.9}$$

The sum of the indices, the molar fractions, is usually normalised to unity. Although, Bragg's rule, is reasonably accurate it is found to deviate by less than 20% from experimentally measured stopping powers. It appears to be in error because the physical and chemical state of the medium are observed to have an influence on the energy loss. The deviation of the Bragg's rule is pronounced around the stopping maximum for light organic gases and for solid compounds containing heavier constituents. Further, any bonding differences between elemental and compound

targets might affect the accuracy of Bragg's rule. In an attempt to improve the accuracy of predicting the stopping powers in compounds, the Köln group (University of Köln), introduced the cores and bonds (CAB) model. This model which is discussed by Ziegler and Manoyan, [Zie88], assumes that the energy loss of ions in compounds is due to two factors: The effect of the closed shells of atoms, cores, and the contribution of the chemical bonds in the material. The difference between the Bragg's rule and the CAB model reduces and ultimately vanishes for projectile velocities above $10v_0$.

3.3 ENERGY STRAGGLING

An energetic projectile ion loses energy by various individual encounters as it traverses a material. Thus, a beam of identical ions with the same incident energy bombarded into the same material will not have the same energy after travelling a distance, Δx, inside the material. This implies that the energy loss, ΔE, is subject to statistical fluctuations. The statistical fluctuation in the energy loss is called energy straggling, and it is illustrated in figure 3.3. Energy straggling tends to limit the precision with which certain information can be retrieved by backscattering spectroscopy. Among other things, depth determination is also impaired by the limited precision of energy loss caused by the effect of energy straggling. The accuracy of the information obtained by backscattering spectroscopy can be improved if quantitative information of the magnitude of the energy straggling for any combination of projectile, target material, target thickness and projectile energy is known.

Bohr, having worked on the theory of electronic energy loss realised the influence of straggling on the result obtained by backscattering spectrometry. Using the same classical model he employed to derive the electronic energy loss formula [Boh48][Chu78], Bohr derived the formula for energy straggling to be:

$$\Omega_B^{\,2} = 4\pi (Z_1 e^2)^2 Z_2 N \Delta x \tag{3.10}$$

Where Ω_B is the standard deviation, and Ω_B^2 is the variance of the energy loss distribution. The above formula only holds in the Bethe-Bloch region, for a Gaussian energy loss distribution. At energies in the vicinity of the maximum of the energy loss curve, the concept of a fully ionised projectile is no longer valid, and the Bethe-Bloch formulation no longer holds. Consequently, the Bohr straggling goes into error. To account for this Lindhard and Scharff extended the work of Bohr to establish the energy straggling in the regions of low and intermediate energies. Their work is discussed in references [Tes95][Chu78][Lin53]. In the light of their work the expression for the energy straggling becomes, where B is the "atomic stopping factor":

$$\Omega^2 = \frac{1}{2}\Omega_B{}^2 \cdot B(\kappa), \kappa \leq 3 \tag{3.11a}$$

and,

$$\Omega^2 = \Omega_B{}^2, \kappa > 3, \tag{3.11b}$$

where,

$$\kappa = \frac{v_1{}^2}{Z_2 v_0{}^2} \tag{3.11c}$$

The above discussion on energy straggling focuses on elemental materials, for straggling in compounds a simple linear additivity of energy straggling is proposed in [Chu76], and can be summarised as follows:

Let's consider a compound mixture of A_mC_n, with atomic density N^{AC}, and the components having densities N_A and N_C, respectively. If it is further assumed that the energy straggling of the components in traversing a depth Δx is given by the Bohr formulation then:

$$\left(\Omega_B^A\right)^2 = 4\pi(Z_1 e^2) Z_A N_A \Delta x \tag{3.12a}$$

$$\left(\Omega_B^C\right)^2 = 4\pi(Z_1 e^2) Z_C N_C \Delta x \tag{3.12b}$$

where in these two equations Z_A and Z_C are the atomic numbers of the components A and C respectively. After a few simple mathematical steps the energy straggling for the compound $A_m C_n$ is determined to be:

$$\frac{\left(\Omega_A^{AC}\right)^2}{N^{AC}} = \frac{m\left(\Omega_B^A\right)^2}{N_A \Delta x} + \frac{n\left(\Omega_B^C\right)^2}{N_C \Delta x} \tag{3.13}$$

The above equation allows the assumption of additivity for energy straggling in a compound material.

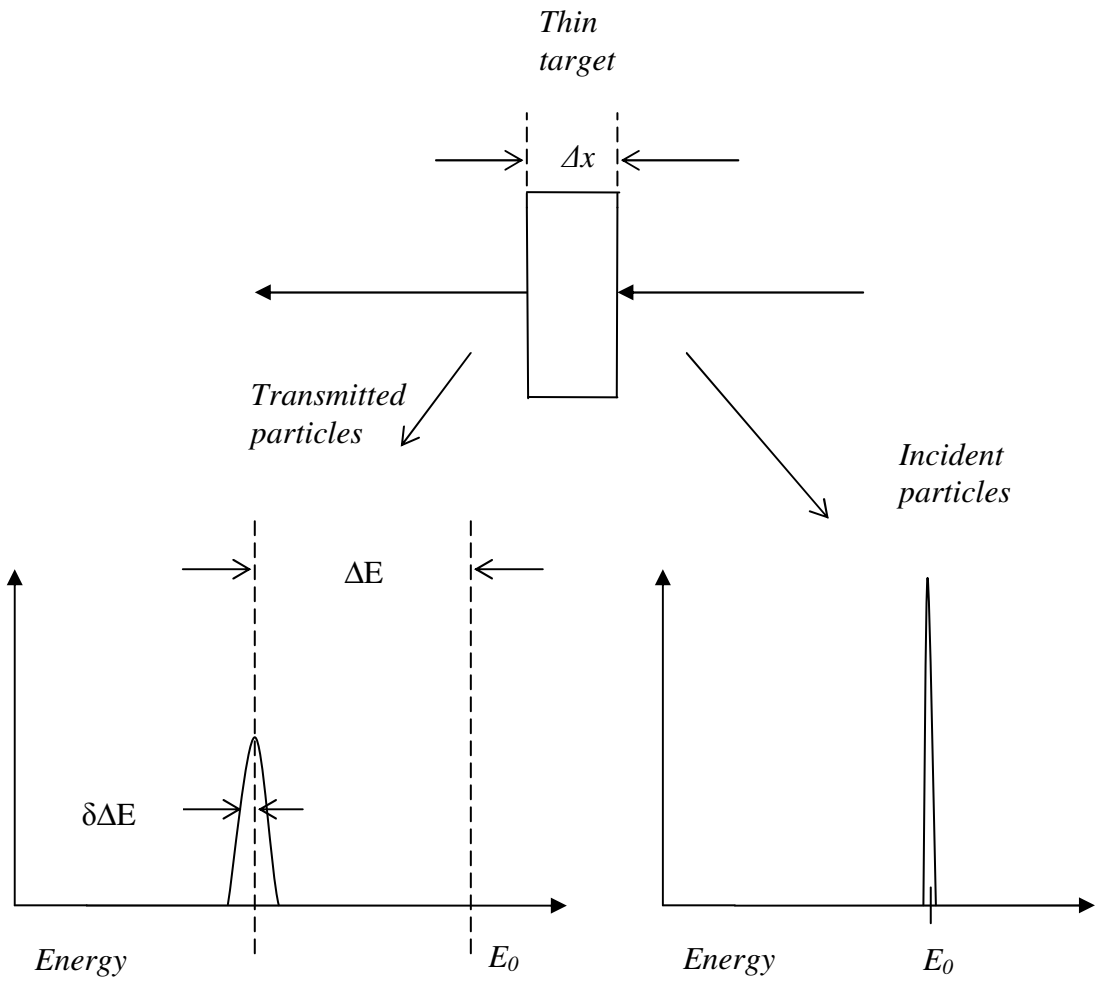

Figure 3.3: A monoenergetic beam of energy E_0 loses energy ΔE in penetrating a thin film of thickness Δx. The effect of energy straggling broadens the energy profile.

3.4 RANGE AND RANGE STRAGGLING

As mentioned in the introductory paragraph of this section, an ion penetrating a material will undergo numerous collisions with the target atoms which will lower its energy, and ultimately cause it to come to rest inside the material. During the collision process, depending on the energy of the ion, the path of the ion will tend to zigzag as it is deflected from one direction to the next. The total distance which the particle travels from incident point on the surface of the material to the point where it is finally imbedded inside the material is the range of the particle. The average range

(usually shortened to just range) of the implanted ions is calculated from knowledge of the stopping power of the target material [Lin63][Car76][Dea73]:

$$R = \frac{1}{N}\int_0^{E_0} \frac{dE}{S_n(E) + S_e(E)} \tag{3.14}$$

Since the stopping power of a material is strongly reliant on the energy of the ion, the range of the ion will also depend primarily on the energy of the ion. The ion range dependence is also based on the individual collision processes underwent by the ion as it penetrates the target material. Thus, identical ions with the same incident energy penetrating the same material will undergo individual and differing collision sequences. This is because the ions have different impact parameters, b, with respect to the target atoms as they penetrate through the material. The fluctuation in the collision sequences will ultimately result in identical ions penetrating the same material being implanted at different depths. The fluctuation of the range about the mean range is called range straggling, ΔR. In addition to the range of the implanted ions we can also define a (average) distance of the ions in the direction perpendicular to the surface, this is known as the projected range, R_p – The projected range is given by the distance of the straight line from the point of incidence on the surface to the point of rest inside the material, figure 3.4. Information about the fluctuations of the projected range with respect to the mean projected range is given by the projected range straggling, ΔR_p.

Ions which have energies within the nuclear stopping domain have an increased chance of colliding with nuclei of the target, which results in many deflections, and thus a projected range which is closer to the surface – figure 3.4. Ions in the electronic stopping domain, on the other hand, tend to have longer projected ranges because the initial penetration of the projectile is controlled by electronic energy losses. The high energy ion will follow a path which is almost a straight line at the beginning because it loses energy to the electrons via excitation and ionization. These processes do not cause a substantial change in direction, they provide a drag to slow the ions down. However, as the projectile ion penetrates deeper into the material it loses energy to the point where nuclear energy loss becomes important, and thus starts to be deflected as would the low energy ion. It is during this period that the path of the ion starts to form

a zigzag pattern, ultimately becoming implanted at some position within the target material – figure 3.4.

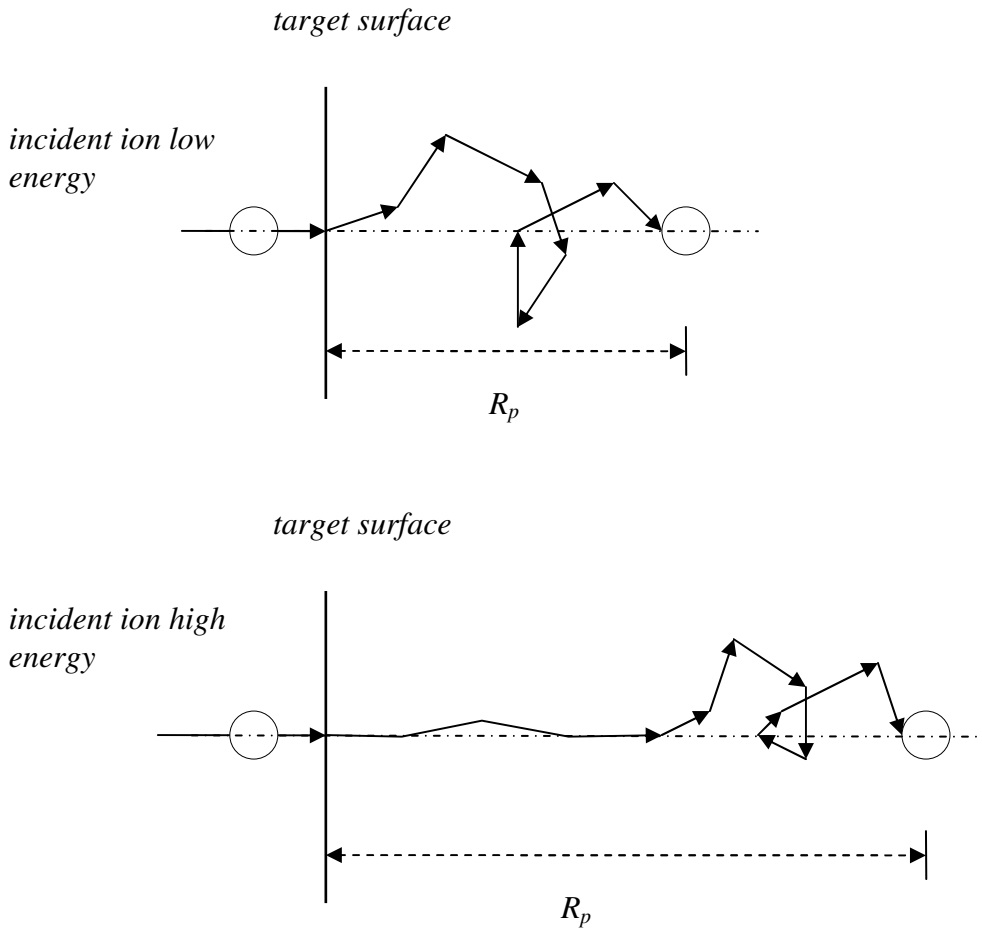

Figure 3.4: A schematic illustration of the motion of an energetic particle penetrating a target material. Top diagram is the motion followed by a low energy projectile. The bottom diagram is the motion of a high energy projectile.

In an amorphous material the atoms are isotropically distributed, the collisions are unrelated thus we can ignore directional effects. The ion implantation profile can be approximated by a Gaussian, with a mean at R_p, and standard deviation given by, ΔR_p:

$$n(x) = n_0 \exp\left(-\frac{(x-R_p)^2}{2\Delta R_p^{\,2}}\right) \qquad (3.15a)$$

In the above equation n_0 is the peak concentration, $n(x)$ is the number of implanted ions at depth x as measured normal to the surface. For a given particle fluence ϕ the peak concentration is given by [www1]:

$$n_0 = \frac{\phi}{\sqrt{2}\Delta R_p} \tag{3.15b}$$

In general the implanted ion distribution deviates slightly from a Gaussian one. In those cases, the distribution of the implanted ions can be characterised by the first four moments: The mean R_p, standard deviation ΔR_p, skewness γ, and its kurtosis β. Skewness gives information about the symmetry of the distribution - For a symmetric distribution the skewness is zero, a right-tailed distribution has a positive skewness and a left-tailed distribution has a negative skewness. Kurtosis indicates the degree of peakedness or flatness of the distribution around the mean. The meaning of the first two moments of a distribution has already been discussed above. At the University of Pretoria the Edgeworth distribution function is used as the fitting function, and it is given by:

$$f(x) = g(x)p(x) \tag{3.16a}$$

where,

$$g(x) = \frac{h}{\sqrt{2\pi}}\exp\left(\frac{-\arg(x)^2}{2}\right) \tag{3.16b}$$

and,

$$p(x) = 1 + \left(\frac{\gamma(\arg(x)^3 - 3\arg(x))}{6} + \left(\frac{(\beta-3)((\arg(x)^4 - \arg(x)^2 + 3)}{24}\right)\right) \tag{3.16c}$$

with,

$$\arg(x) = \frac{(x - R_p)}{\Delta R_p} \tag{3.16d}$$

and h is the height fitting parameter.

Ion ranges in compounds can also be estimated in the same way as required by Bragg's rule for energy straggling:

$$R^{AC} = mR^{A} + nR^{C} \tag{3.17}$$

where A and C are constituents or elements of the compound A_mC_n, and m and n are normalised to unity – they represent the relative compositions of A and C.

3.5 RADIATION DAMAGE

Radiation damage is defined as the redistribution of the target atoms in a crystalline/polycrystalline material due to the transfer of energy from an incident projectile ion. This event is composed of several processes and these include [Was07]:

- The transfer of kinetic energy to the target atoms resulting in a primary knock-on atom.
- The displacement of an atom from its lattice position.
- The passage of the displaced atoms through the lattice and the accompanying creation of additional knock-on atoms.
- Collection of point defects created by the primary knock-on atom.
- The termination of the primary knock-on atom (PKA) as either an interstitial or a substitutional atom.

From the processes outlines above it is clear that the radiation damage event is concluded when the PKA comes to rest in the lattice. The result of a radiation damage event is the creation of a collection of point defects, and clusters of these defects in the crystal lattice. Any other subsequent processes which might occur, e.g. migration

of point defects; defect clusters etc. are classified as radiation damage effects. These effects will largely depend on a number of conditions, i.e. temperature of the system, energy of the projectile, etc.

3.6 ION CHANNELLING

Ion penetration in an amorphous material differs from that in a crystalline material. Ions implanted in a crystalline material tend to have skewed distributions, rather than symmetric distributions as is the case for amorphous materials [Dea73]. This is because in a crystalline material some of the ions travel such that their motion is constrained between closed packed rows of atoms, which in turn results in long range trajectories. The space between the adjacent close packed rows of atoms is referred to as open channels, figure 3.5. The trajectory of the ions travelling through the open channels is controlled by a series of small angle collisions within the atomic rows. This has the consequence that such ions tend to have a reduced energy loss as compared to ions not travelling through such channels, thus the range will be different. The phenomenon where ions travel through closed packed rows and planes of atoms is known as ion channelling.

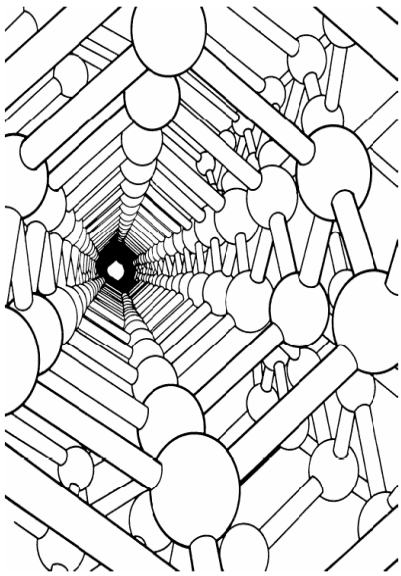

Figure 3.5 : A schematic representation of an open channel. Taken from reference [www1].

For the treatment of channelling in this section four assumptions are necessary: The first assumption requires that the scattering angles be small. This is important since large angle scattering can result in complete loss of direction and the correlation between the collisions becomes less obvious. Since strong collisions require that the interacting particles come close, strong correlations occur if the first assumption holds. Thus, the second assumption requires that if a particle comes close to one atom in a row of atoms it must then also come close to the neighbouring atom in the same row. This leads to the concept of a string of atoms characterised by a separation distance *d,* thirdly, the interaction can be described classically as two body collisions. Lastly, we assume a perfect lattice and a perfect string of atoms.

If the assumptions are taken to hold, then the motion of a particle in a channel can be roughly illustrated by figure 3.6, below. In figure 3.6, the motion of the projectile is a sinusoidal one as a result of the strong correlation between the series of collisions. The walls of the channel are formed by the strings of the atoms as required by the second assumption. Figure 3.6, also contains an illustration of what the potential between the strings of atoms and the particles should be approximated as. As can be seen the potential is zero along the central axis of the channel, which is the line about which the motion of the projectile oscillates. As an additional approximation, it is assumed that the projectile interacts with a single string at a time [Lin65]. Hence, we note that the potential increases as the projectile approaches a single string. In order for the projectile to remain in the channel its maximum radial kinetic energy must not exceed the potential energy.

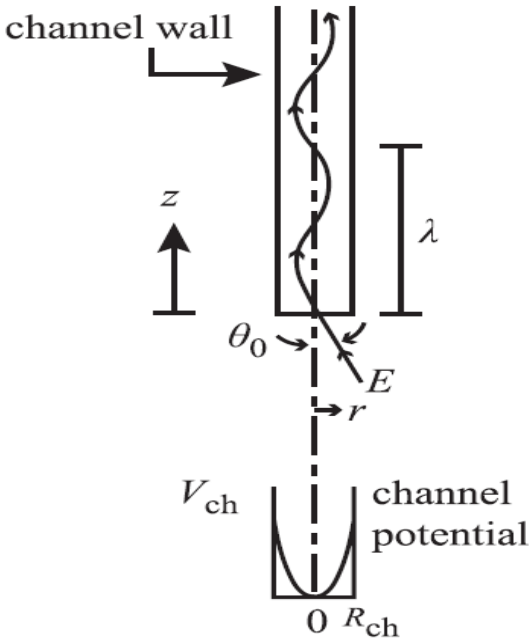

Figure 3.6*: An illustration of the projectile ion trajectory with wavelength λ, inside a channel of width R_{ch}. The second figure is an illustration of the potential V_{ch} due to the strings of atoms. Taken from reference [Was07].*

Using the continuum approximation which follows from the assumption of a string of atoms, that is, the discrete nature of the atomic potential is negligible. The average potential at a distance r from the string of atoms is given by:

$$\overline{U}(r) = \frac{1}{d}\int_{-\infty}^{\infty} V(\sqrt{r^2 + z^2})dz \tag{3.18a}$$

where z is the distance travelled along the string of atoms, d is the between the separation between the atoms, $V(\sqrt{z^2 + r^2}) = V(R_i)$ is the ion-atom potential, and R_i is the ion-atom separation. An extensive treatment of channelling theory is given in [Lin65], where also an ion-atom potential within the Thomas-Fermi treatment is established to be:

$$V(R_i) = \frac{Z_1 Z_2 e^2}{R_i}[1 - \frac{1}{(R_i^2 + (Ca_{TF})^2)^{1/2}}] \tag{3.18b}$$

where $a_{TF} = 0.46(Z_1^{2/3} + Z_2^{2/3})^{-1/2}$ Å is the interatomic potential screening length of the ion-atom interaction, Z_1 and Z_2 are the ion and string atom atomic numbers, respectively, and C is an adjustable parameter usually taken as $C \approx \sqrt{3}$ to give a fairly good over-all fit. Substituting equation (3.18b) into equation (3.18a) and evaluating the integral the average potential becomes:

$$\overline{U} = \frac{Z_1 Z_2 e^2}{d} \ln\left[\left(\frac{a_{TF} C}{r}\right)^2 + 1\right] \tag{3.18c}$$

Given that the projectile enters a channel at some angle θ_0 to the central axis of the channel as can be seen in figure 3.6, the radial velocity component of the projectile becomes:

$$V_{0r} = \left(\frac{2E_1}{M_1}\right)^{1/2} \sin\theta_0 \tag{3.19a}$$

where E_1 is the total kinetic energy of the particle, M_1 is the mass of the projectile. The radial kinetic energy of the projectile is thus given by:

$$K = \frac{1}{2} M_1 {V_{0r}}^2 = E_1 {\theta_0}^2 \tag{3.19b}$$

In the above equation θ_0 is assumed to be very small. As stated before the projectile will exit the channel provided its radial kinetic energy exceeds the potential barrier provided by the string of atoms. As can be seen from the latter equation above the radial kinetic energy has a dependence on the angle the projectile makes with respect to the central axis of the channel. By comparing the kinetic energy and the potential energy the critical angle for channelling to occur is determined to be:

$$\psi_c \cong \left(\frac{2Z_1 Z_2}{E_1 d} \right)^{1/2} \tag{3.20}$$

from the above equation, the critical angle depends on the atomic species and on the energy of the projectile. Thus, channelling is most likely for heavy ions and for ions with comparatively low energy. By low energy, however, it is not meant energies where nuclear stopping is important. For mixed strings of different atoms, Z_2 is an arithmetic mean of the atomic numbers of the atoms in the string. If the atoms are not uniformly spaced along the string, d is also taken as an average spacing [Wan09]. Tables of data exist with factors with which to multiply the lattice constants to give the different atomic spacing inter-planar spacing in common diatomic compounds [Wan09] and [Chu78].

3.7 SIMULATIONS WITH THE STOPPING AND RANGE OF IONS IN MATTER

SRIM is a group of programs which are used to calculate the stopping and range of ions in matter. These programs are based on a Monte Carlo simulation method – the binary collision method. The TRIM program within SRIM is designed to calculate the distribution of ions inside an amorphous target [Zie85]. The basic assumptions that the SRIM program makes when simulating a distribution of ions are as follows:

- The interaction of the ion and atoms is a binary. The influence of the neighbouring atoms is ignored.
- The potential of interaction between the ion and atom has a universal form. And has been established to be an average fit to quantum mechanical considerations.
- The SRIM program does not take into account the crystal structure nor any dynamic changes in the material during the implantation process.
- As a consequence, the recombination of the vacancies and interstitials is also ignored.

The program with all its assumption still maintains a reasonable level of accuracy with approximately 5 – 10 % error. The TRIM program has been designed to include the “CAB” model corrections to the Bragg’s rule of compound stopping power [www3][Zie10].

3.8 REFERENCES

[Bet30] H. Bethe, Ann. Phys. (Leipzig) **5** (1930) 324.

[Blo33] F. Bloch, Ann. Phys. (Leipzig) **16** (1933) 285.

[Boh13] N. Bohr, Phil. Mag. **25** (1913) 10.

[Boh48] N. Bohr, Matt. Phys. Medd. Dan Vid. Selsk., **24** (1948) 19.

[Bra05] W.H. Bragg, and R. Kleeman, Phil. Mag. **10** (1905) 318.

[Car76] G. Carter, W.A. Grant, (1976). "Ion Implantation", Edward Arnold (Publishers), London.

[Chu76] W.K. Chu, Phys. Rev. A **13** (1976) 2057.

[Chu78] W.K Chu, J.W Mayer and M.A Nicolet, (1978). ''Backscattering Spectroscopy", Academic Press.

[Dea73] G. Dearnerly, J.H. Freeman, R.S. Nelson, and J. Stephen, (1973). "Ion Implantation" North Holand Publ., Amsterdam.

[Fir59] O.B. Firsov, Zh. Eksp. Teor. Fiz. **36** (1959) 1517.

[Lin53] J. Lindhard, and M. Scharff, and H.E. Schiøtt, Mat. Fys. Medd. Dan. Vid. Selsk. **27** (1953) 15.

[Lin61a] J. Lindhard, and M. Scharff, Phys. Rev. **124** (1961) 128

[Lin61b] J. Lindhard, M. Scharff, and K. Dan,Vidensky. Selik. Mat. Fys. Medd., **33** (1961) 14.

[Lin63] J. Lindhard, and M. Scharff, and H.E. Schiøtt, Mat. Fys. Medd. Dan. Vid. Selsk. **33** (1963) 14.

[Lin65] J. Lindhard, Mat. Fys. Medd. Dan. Vid. Selsk. **34** (1965) (14) 1.

[Tes95] J.R. Tesmer, and M. Nastasi, (Eds)., (1995). "Handbook of Modern Ion Beam Analysis." Materials Research Society, Pittsburg, Pennsylvania.

[Wan09] Y. Wang, and M. Nastasi,(Eds)., (2009). "Handbook of Modern Ion Beam Analysis." Materials Research Society, Pittsburg, Pennsylvania.

[Was07] G.Was, (2007). "Fundamental of Radiation Materials Science", Springer-Verlag Berlin Heidelberg.

[www1] http://personal.cityu.edu.hk/~appkchu/AP4120/9.PDF - 2013/05/22.

[www2] ocw.mit.edu/courses/nuclear-engineering/22105...fall.../chap6.pdf - 2013/11/12.

[www3] http://www.srim.org/SRIM/Compounds.htm - 2014/01/08.

[Zie10] J.F. Ziegler, M.D. Ziegler, and J.P. Biersack, Nucl. Instr. and Meth. **B 268** (2010) 1818.

[Zie85] J. F. Ziegler, J. P. Biersack and Y. Littmark, (1985). "The Stopping and Range of Ions in Solids", Pergamon Press.

[Zie88] J.F Ziegler and J.M Manoyan, Nucl. Instr. and Meth. **B35** (1988) 215.

[Zie99] J.F. Ziegler, J.App. Phys. Rev. **85** (1999) 1249.

CHAPTER 4 ANALYSIS TECHNIQUE

Chapter 3 discusses ion implantation and the detailed processes that govern the procedure. The fundamental part of this project was to assess the distribution of the implanted Kr ions and to monitor the change in the Kr depth profile when the SiC-substrate was subjected to a series of heat treatments. Rutherford Backscattering Spectroscopy (RBS) is a widely used technique for analysis of depth distributions of implanted ions. It was used as an analysis technique for this project largely because of its good depth resolution and depth profiling of individual elements, it is also quick and easy to use allowing a number of measurements to be done on a single day. In addition to the above mentioned properties of the technique, RBS is also a widely preferred technique because of its comparatively non-destructive nature, and quantitative determination of material composition.

4.1 OPERATING PRINCIPLE OF RBS

The technique is based on the concept of ion scattering by an atomic nucleus. This concept was developed by nuclear physicists after Rutherford proposed his theory of the atomic structure.

A beam of energetic charged particles (He-ions) is produced with the aid of an ion source and a particle accelerator. A Van de Graaff accelerator was used in this project. Once a straight beam is produced, a magnetic field is applied to bend the beam, which also acts as a filter and selects only particles with a certain energy and mass. The energetic ions are further passed through a series of collimation slits prior to reaching the analysis chamber. The accelerating tube is fitted with a vacuum pump to minimise any scattering by air. A collimated and mono-energetic beam of particles reaches the chamber and impinges on the target substrate – SiC implanted with Kr-ions. We assume that the sample is thick enough, such that only particles scattered through an angle greater than 90^{o} can be detected. This consequence is what gives the technique its name: “back-scattering”. The analysis chamber houses a solid-state detector which relays the information of the backscattered particles as an electrical signal, which is

then processed by the analog and digital electronics. The analog signal is converted into a digital signal by a multi-channel analyser: The multi-channel analyser receives an analog signal from the amplifiers, depending on its magnitude the signal is recorded in a storage cell. Each cell is numbered and referred to as a channel. The multi-channel analyser contains many such channels, and each one has a finite width, ξ (Energy/channel), whose magnitude depends on the system calibration. It is typically around 3 (keV/channel). Any event which is recorded into a particular channel is called a count. At the end of the data collection process each channel registers a certain number of counts, and a spectrum of counts per channel vs. channels is obtained, figure 4.1. Counts per channel are also referred to as a backscattering yield. The data is then stored in a computer as a digital spectrum (Backscattering spectrum) ready for analysis. There is a relationship between the channel numbers and the energy of the detected particle energy. This is usually determined experimentally, and is under ideal conditions given by a linear relationship between the channel numbers and the detected particle energy, with the channel width, ξ, expressed as the slope, figure 4.2. Complete understanding of how to read and interpret the generated backscattering spectrum relies on the knowledge of the physical processes governing the RBS technique. These include the kinematic factor, scattering cross-section, and depth scaling as will be discussed below. Knowledge of these physical processes allows us to identify elemental composition of samples, perform depth profiling etc.

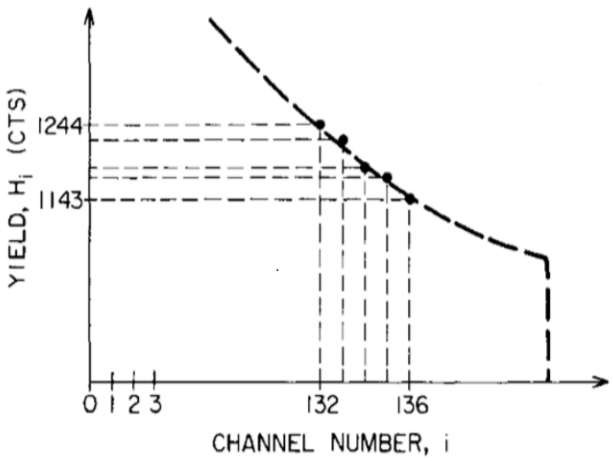

Figure 4.1: A typical backscattering spectrum as obtained from the computer in terms of counts per channel and channel number. Taken from reference [Chu78].

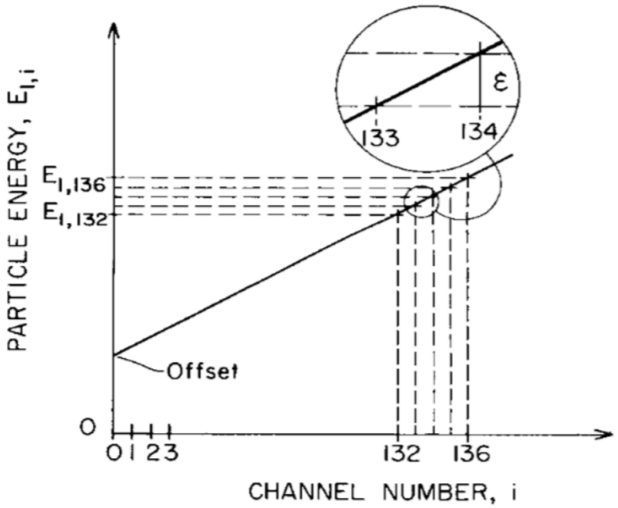

Figure 4.2: The relationship between channel number and detected particle energy is linear. The slope gives the width of an individual channel and also the offset is given. Taken from reference [Chu78].

4.2 PHYSICAL PROCESSES

4.2.1 KINEMATIC FACTOR

One of the quality aspects of RBS is its ability to determine material composition. This is a consequence of the nature of the backscattering events; atoms backscattered from different masses at the same position will possess different energies. The information about the masses of atoms in a material, and hence its composition is contained in the kinematic factor K:

$$K = \frac{E_1}{E_0} \tag{4.1}$$

The kinematic factor is a proportionality constant between the backscattered ion energy E_1 and the incident ion energy E_0 on a surface target atom of particular mass.

To avoid the effects of energy-straggling this discussion is limited to ions backscattered from the target surface.

The kinematic factor is established by considering a classical two body collision between a projectile ion and a target atom. The projectile ion approaches the target with incident energy E_0. It collides and transfers some of its energy to the target atom causing it to recoil at some angle α. The collision also results in a deflection of the projectile through an angle θ to the incident direction. If the collision is an elastic one, that is, both the kinetic energy and momentum of the system are conserved, the kinematic factor can be computed as a function of the projectile mass M_1, target atom mass M_2 and deflection angle θ:

$$K = \left[\frac{\left(M_2^{\,2} - M_1^{\,2} \sin^2 \theta\right)^{1/2} + M_2 \cos\theta}{M_1 + M_2} \right]^2 \tag{4.2}$$

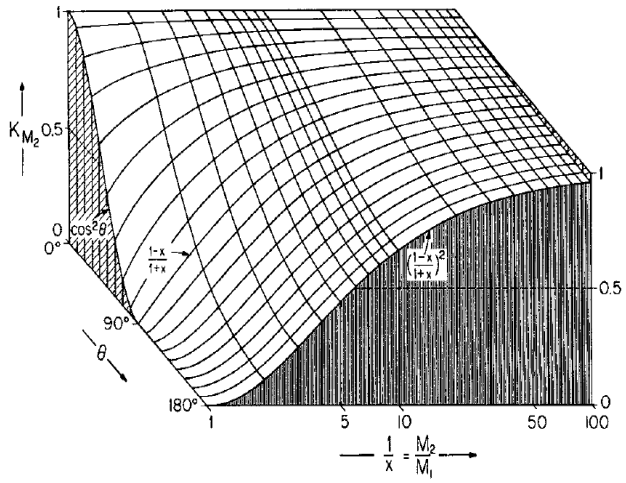

Figure 4.3: The kinematic factor plotted as a function of the scattering angle and the ratio of the target atom mass to the projectile ion mass. K_{M2} is the kinematic factor with the subscript emphasizing the mass of the target atom M_2, and x is the ratio of the projectile ion mass, M_1, to that of the target atom, M_2. Taken from reference [Chu78].

This figure summarises all the information concerning the kinematic factor and its relationship to the scattering angle and the ratio of the target atom mass to the projectile ion mass. Firstly, it is important to note that the kinematic factor is zero for angles greater than 90^o when the projectile's mass is equal to the target atoms' mass. It follows from this observation that there is no backscattering of any ions when the projectile's mass is equal or greater than that of the target atom's. Furthermore, it is evident that the projectile ions backscattered from atoms with a greater mass will be backscattered at higher energies, since the kinematic factor increases with increasing target atomic mass. It is this result which makes RBS a powerful analytical technique for target composition determination. A problem however, is encountered if the target analysed is made up of two atomic species with masses that are close to each other.

From equation (4.1) and (4.2), if θ is fixed, the relationship between the energy difference ΔE_1 and the target mass difference ΔM_2 is given by:

$$\Delta E_1 = E_0\left(\frac{dK}{dM_2}\right)\Delta M_2 \qquad (4.3a)$$

The distinction between any two atoms can be made under the condition that the difference in mass ΔM_2 gives rise to a difference in the detected energies that is greater than the minimum energy difference that can be experimentally resolved by the detector, δE. It is important to realise at this point that for this discussion only contributions from the surface atoms are considered, thus energy straggling and other factors which rely on the ion's interaction with the bulk of the material are not important. Only the system resolution has influence on δE. For a fixed $\delta E/E_0$ the following relationship contains information about the state of the system mass resolution:

$$\delta M_2 = \frac{\delta E}{E_0}.\frac{1}{(dK/dM_2)} \qquad (4.3b)$$

Equation (4.3b) and figure 4.4 contain information about the mass resolution of the system for a fixed scattering angle, θ, and ratio $\delta E/E_0$ – The notation in equation (4.3a) gives the general relationship between the change in mass, ΔM_2, and change in

energy, ΔE_1, whereas the notation in equation (4.3b) emphasises the minimum detectable change in mass, δM_2, and minimum energy difference, δE, detectable. By increasing the change in the kinematic factor with a small change in atomic mass, dK/dM_2, the mass resolution can be improved considerably. From figure 4.4 it is evident that for light projectile ions the mass resolution is optimal for light target atoms. Also from the same figure it is noted that mass resolution can be improved for relatively heavier target atoms by using comparatively heavier projectile ions. In addition to the conclusions drawn from figure 4.4, equations (4.3a) and (4.3b) further imply that the mass resolution could also be improved by increasing the incident ion energy E_0.

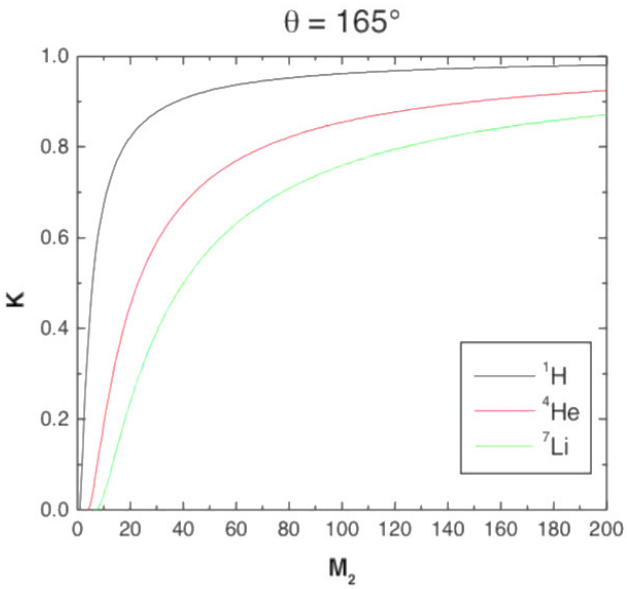

Figure 4.4: Kinematic factor as a function of target atomic mass at an angle of $\theta = 165^o$ for Hydrogen, Helium and Li atom as projectile ions. Taken from reference [www1].

4.2.2 DEPTH SCALE

As a beam of particles impinges on the surface of the target material some particles backscatter, their energy is given by equation (4.1). However, some of the beam particles probe through the material until they eventually backscatter at some depth x. The fate of these particles is strongly determined by the stopping power of the

material. When these particles backscatter at the depth x they have energy E (just before the collisions takes place) that is less than the surface incidence energy, E_0:

$$E = E_0 - \int_0^{x/\cos\theta_1} \frac{dE}{dx'} dx' \tag{4.4a}$$

The integral is evaluated from the surface at $x' = 0$ to $x' = x/\cos\theta_1$. It is important to note that the integral is not taken at $x' = x$, rather at $x' = x/\cos\theta_1$ this is because the incidence angle is θ_1 therefore the total path length is $x/\cos\theta_1$, where x is only the perpendicular distance – Parallel to the normal of the surface. Figure 4.5 gives a schematic illustration of the scenario. After scattering at depth x inside the material the projectile continues to lose energy as it travels out of the material. The energy that is read by the detector is given by:

$$E_1 = KE - \int_0^{x/\cos\theta_2} \frac{dE}{dx'} dx' \tag{4.4b}$$

This integral is evaluated over a total length of $x/\cos\theta_2$. KE is the energy of the projectile immediately after scattering at depth x. These equations cannot be evaluated since the stopping is known only as a function of energy.

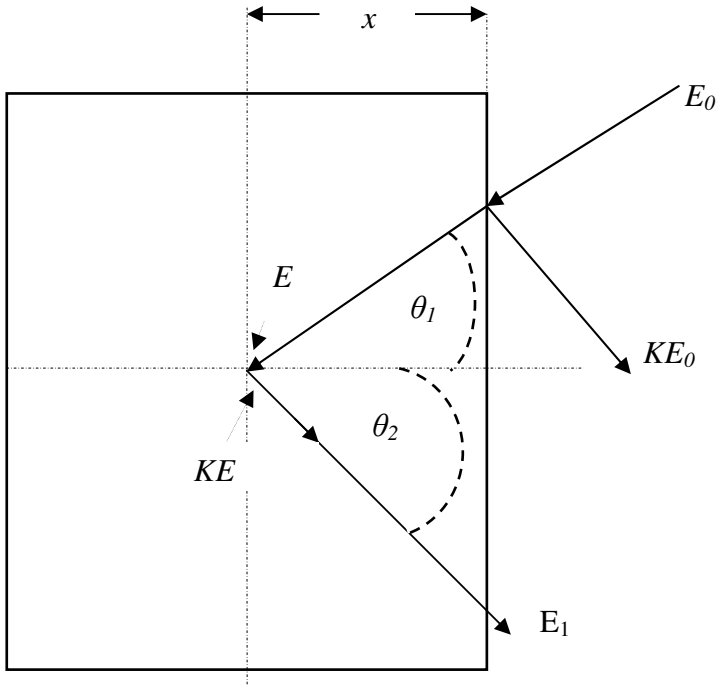

Figure 4.5: Schematic diagram displaying backscattering events in an elemental target.

Equations (4.4a) and (4.4b) require knowledge of the specific energy loss, *dE/dx*, as a function of *x*. However, the only information that is available is the stopping power as a function of energy, *E*. Therefore, the equations are re-written as follows:

$$\frac{x}{\cos\theta_1} = \int_{E}^{E_0} \frac{dE'}{(dE'/dx)} \tag{4.5a}$$

This integral is evaluated from *E* to E_0, since $E_0 - E$ is the energy difference as along the inward path. Since the upper limit is fixed, it is evident that *x* increases as *E* decreases. Likewise, equation (4.4b) is also re-written as:

$$\frac{x}{\cos\theta_2} = \int_{E_1}^{KE} \frac{dE'}{(dE'/dx)} \tag{4.5b}$$

The integral is evaluated from E_1 to *KE*, since $KE - E_1$ is the energy lost along the outward path. It is very important to note that the stopping for the inward travel is

different from the stopping power for the outward travel. This is due to the energy dependence of the stopping power. In this new formulation, the integrand is no longer the specific energy loss, rather its inverse *dx/dE*. Figure 4.6 shows the dependence of the inverse stopping power on energy.

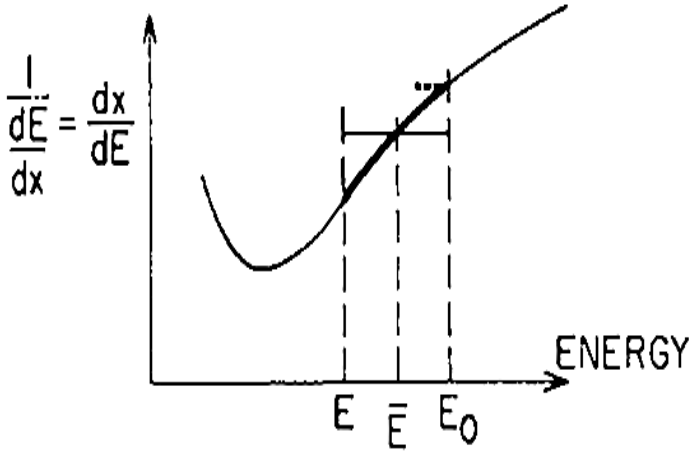

Figure 4.6: Energy dependence of the inverse of the energy loss factor. Taken from reference [Chu78].

One method of evaluating the integrals is to assume that *dE/dx* is constant along the inward and outward paths. This method has the advantage of simplifying the integrals, which results in:

$$E = E_0 - \frac{x}{\cos\theta_1}\frac{dE}{dx}(in) \tag{4.6a}$$

and,

$$E_1 = KE - \frac{x}{\cos\theta_2}\frac{dE}{dx}(out) \tag{4.6b}$$

Distinction is made between the energy loss for the inward path and the specific energy loss for the outward path. By eliminating *E* in the two equations and taking the

difference between the energy of the particles that scatter from the surface and the energy of the particles that scatter from a depth *x*:

$$\Delta E = KE_0 - E_1 = \left[\frac{K}{\cos\theta_1}\frac{dE}{dx}(in) + \frac{1}{\cos\theta_2}\frac{dE}{dx}(out) \right] x \qquad (4.7a)$$

$$\Delta E = N[S]x \qquad (4.7b)$$

This method results in a linear relationship between the energy difference of the particles and the depth inside the material where the particles scatter. The constant of linear proportionality is referred to as the stopping power factor, *[S]*.

The above results are a consequence of the assumption that the stopping power can be treated as a constant. There are other methods which could be used to evaluate the integrals; these include numerical and analytical methods which will not be discussed in this section. However, for anyone who is interested in such methods there is an excellent summary of such techniques in the book by reference [Chu78].

The above analysis has been done for a purely elemental sample. In the case of a compound, the mathematics is still the same only we change the notation slightly to account for the different atoms in the sample. The backscattering energy of the projectile depends on the type of atoms it scatters from. If we consider a compound A_mC_n, in the atomic ratio *m/n* – then the energy of the projectile that scatters from the surface atoms becomes:

$$E_A = K_A E_0 \qquad (4.8a)$$

or,

$$E_C = K_C E_0 \qquad (4.8b)$$

Which one is recorded at the detector will depend on the scattering atom. K_A and K_C are the kinematic factors of the scattering atoms, A and C, respectively. The particles which probe into the material will lose energy as a consequence of interacting with different atoms. The stopping power for the compound, A_mC_n, as given by Bragg's rule is:

$$S^{A_mC_n} = mS^A + nS^C \tag{4.9}$$

The energy loss that a particle penetrating through the material incurs is given by:

$$\Delta E_{in} = \frac{N^{AC}x}{\cos\theta_1} S_{in}^{AC} \tag{4.10}$$

N^{AC} is the number of molecules A_mC_n per unit volume, and S_{in}^{AC} is the stopping cross-section for the inward path. The energy loss on the outward path depends on the type of scattering atom. The energy difference between the particle that scattered from the surface atoms and the particles that penetrates and scatters at a depth x is given by:

$$\Delta E_A = \left[S_A^{AC}\right] N^{AC} x \tag{4.11a}$$

and,

$$\Delta E_C = \left[S_C^{AC}\right] N^{AC} x \tag{4.11b}$$

where,

$$\left[S_A^{AC}\right] = \frac{K_A}{\cos\theta_1} S_{in}^{AC} + \frac{1}{\cos\theta_2} S_{out,A}^{AC} \tag{4.12a}$$

$$\left[S_C^{AC}\right] = \frac{K_C}{\cos\theta_1} S_{in}^{AC} + \frac{1}{\cos\theta_2} S_{out,C}^{AC} \tag{4.12b}$$

The superscripts represent the stopping material, and the subscripts represent the scattering atom. The above formulation implies that for a compound sample we should have two depth scales. However, the two depth scales are not different by more than 10% in most cases of mega-electron volts of ^{4}He [Chu78]. Since they were both established for the case of a constant stopping power the individual depth scales can also be assumed to be linear. Although the set of established equations and relationships are enough to perform depth profiling in backscattering analysis, a problem usually arises when the ions scatter from depths that are very close to each other. From equation (4.7b), it is seen that the minimum detectable depth difference, δx, can be related to the minimum detectable scattered particle energy difference, δE, by [Wan09]:

$$\delta x = \frac{\delta E}{N[S]} \tag{4.13}$$

A common practise to improve depth resolution is by increasing the stopping power factor, $[S]$. This is done by tilting the sample normal relative to the incoming beam of ions, giving an increase in θ_1. This effect increases the path length required to reach a given depth, thus increasing the energy difference of the scattered particle for a given depth difference. This method however requires that the material be reasonably flat [Wan09].

4.2.3 RUTHERFORD SCATTERING CROSS-SECTION

The idea of scattering cross-section is obtained from the classical picture of scattering: A body which is bombarded by energetic particles will scatter all the particles which move within the area covered by the body. The particles will be scattered in different directions, and each direction is associated with a certain area portion of the entire body. Particles incident within an infinitesimal spot of differential cross-sectional area, $d\sigma$, will scatter into a corresponding infinitesimal differential solid angle $d\Omega$. A solid angle is the two dimensional angle in three dimensional space which is subtended by a point. The ratio of these infinitesimal quantities, $d\sigma/d\Omega$, is called the differential scattering cross-section. The differential scattering cross-section is related

to the probability of a scattering event into a particular direction, since the greater the cross-sectional area, $d\sigma$, the better is the chance of scattering in the corresponding direction. This concept has a direct relation to the RBS technique because it is important to know the probability of particles scattering into the detector.

Rutherford established the differential cross-section of scattering through an angle θ during an elastic collision between charged particles in a Coulomb potential to be [www2]:

$$\frac{d\sigma}{d\Omega} = \left(\frac{Z_1 Z_2 e^2}{4E_1 \sin^2 \theta} \right)^2 \frac{4\left\{ \left[1 - \left((M_1/M_2) \sin\theta \right)^2 \right]^{1/2} + \cos\theta \right\}}{\left[1 - \left((M_1/M_2) \sin\theta \right)^2 \right]^{1/2}} \tag{4.14}$$

From the above formulation a few conclusions can be made concerning the differential scattering cross-section:

- $d\sigma/d\Omega$ is proportional to Z_1^2 and Z_2^2, the projectile atomic number and the target atomic number. This has the consequence that for any given projectile ion RBS is more sensitive to heavier atoms than it is to lighter ones.
- $d\sigma/d\Omega$ is inversely proportional to the square of the projectile energy E_1, thus there is higher backscattered yield for low energy ions than there is for high energy ions.

In an RBS setup where you have an incident beam of particles on a target material of density N, and thickness t, the number of particles which reach the detector with solid angle Ω is:

$$A = \sigma \Omega Q N t \tag{4.15}$$

where, Q, is the number of particles incident on the material, Nt, is the number of scattering centres in the material, and σ is the average scattering cross-section expressed as:

$$\sigma = \frac{1}{\Omega}\int_{\Omega}\frac{d\sigma}{d\Omega}d\Omega \tag{4.16}$$

4.3 SPECTRUM HEIGHT

The section on depth scaling discussed the relationship between the energy of the backscattered particles and the depth within the target where the scattering occurs. This section discusses the relationship between the height of the backscattering spectrum and the number of scattering centres per unit area within the sample where the backscattering events occur. The height of a backscattering spectrum is the number of counts recorded into a particular channel *i*. In accordance with the channel width, ξ, particles with an energy difference equal to the channel width will all be recorded in the same channel *i*. This has the implication that each channel *i* can be linked to some thickness, t_i, in the sample which gives an energy difference, ξ,:

$$\xi = [S]Nt_i \tag{4.17}$$

In equation (4.17) above, *[S]* is the stopping power factor and *N* is the atomic density of the material. According to equation (4.15) the number of particles scattered from a thickness t_i into the solid angle, Ω, is given by:

$$H_i = (\sigma\Omega N t_i)/[S]\cos\theta_1 \tag{4.18a}$$

where *Q* is the number of incident particles, σ is the scattering cross-section, Ω is the detector solid angle. In accordance with equations (4.17) and (4.18a) the surface spectrum height can be obtained from:

$$H_0 = (\sigma\Omega Q)\xi/[S]\cos\theta_1 \tag{4.18b}$$

All the quantities in equation (4.18b) are evaluated at the incident energy, E_0, in accordance with the surface energy approximation. The spectrum height as obtained

for scattering from some depth x within the sample is more involved, and its derivation will not be given here, only the expression:

$$H(E_1) = \sigma(E) Q \Omega \xi \frac{S(KE)}{[S(E)]\cos\theta_1 S(E_1)} \tag{4.18c}$$

where E_1 is the detected energy, E is the energy just before the scattering occurs, and KE is the energy immediately after scattering at the depth x. For the details of the derivation of equation (4.18c), see ref. [Chu78] or [Fen73].

The above formulas can be generalised to give the spectrum height for two elemental peaks in a compound A_mC_n in the following way:

The surface spectrum heights for two elemental peaks in a compound A_mC_n are given as:

$$H(E_0)_A = \sigma_A(E_0) \Omega m \xi / [S(E_0)]_A^{AC} \cos\theta_1 \tag{4.19a}$$

and,

$$H(E_0)_C = \sigma_C(E_0) \Omega n \xi / [S(E_0)]_C^{AC} \cos\theta_1 \tag{4.19b}$$

The subscripts give the scattering atoms, and the superscripts give the stopping medium. The position of the edge of each signal is determined by the kinematic factor such that the heavier atom always occurs at a high energy. However, if there is an overlap between the signal of the heavy and light atoms, the spectrum height at that particular energy is given by:

$$H(E_1) = H_A(E_1) + H_C(E_1) \tag{4.20}$$

Where E_1 gives the energy of the channel at which the overlap occurs. In the case that the overlap is at some depth x, then the individual spectrum height will be given by:

$$H(E_1)_A = \sigma_A \Omega Q \xi n \frac{S_A^{AC}(K_A E_{A)}}{[S(E_A)]_A^{AC} S^{AC}(E_1)} \tag{4.21a}$$

and,

$$H(E_1)_C = \sigma_C \Omega Q \xi n \frac{S_C^{AC}(K_C E_{C)}}{[S(E_C)]_C^{AC} S^{AC}(E_1)} \tag{4.21b}$$

The definition of the variables is similar to the case of a single elemental sample, only now the subscripts give the scattering atom and the superscripts give the stopping material.

4.4 RUTHERFORD BACKSCATTERING SPECTROSCOPY WITH CHANNELLING (RBS – C)

Ion channelling is a powerful technique for the characterisation of crystalline solids. The method is based on the channelling effect, which as described in chapter 3, is the steering of a well collimated energetic beam of particles through close packed rows and planes of atoms. This steering avoids close encounters with the atoms in the close-packed rows and planes as a consequence there is a reduced yield in the backscattering spectrum. The spectrum obtained via this channelling process is referred to as an aligned yield, where the yield collected without aligning the energetic beam of particles along any crystallographic direction is referred to as a random spectrum. There are two types of channels, axial and planar channel. For this project, however, the axial-type channelling was used as a consequence the discussion in this section will be based on the axial-type channelling measurements.

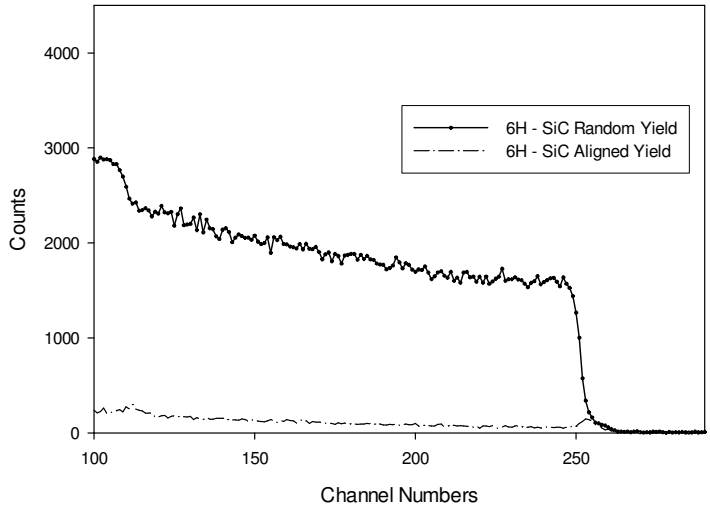

Figure 4.7: A schematic representation of the aligned (dashed line) and random spectra obtained from a 6H-SiC sample bombarded with mono-energetic He ions.

As can be seen from figure 4.7 above there is a significant decrease in the yield for a beam of particles aligned with the crystallographic direction of a crystal. In the aligned spectrum of figure 4.7 a clear resolvable surface peak can be seen. The surface peak is due to scattering from the outermost atoms of the material. This scattering could be due to lattice vibrations, a shift in the lattice position caused by surface reconstruction and/or surface relaxation. Another factor which might affect the surface peak is the presence of contaminants on the surface of the sample, usually a surface oxide layer. The latter contribution is reduced by cleaning the sample thoroughly and taking the RBS measurements in a high vacuum. The channelling effect is characterised by a critical angle, $\psi_{1/2}$, and a minimum yield, χ_{min}. The critical angle as derived by Lindhard [Lin65] is given as:

$$\psi_c = \left(\frac{2Z_1 Z_2 e^2}{Ed} \right) \tag{4.22}$$

E is the ion incident energy, *d* is the atomic spacing along the axial direction, all other symbols have the obvious meaning as already defined. The critical angle is the angle at which the distance of closest approach between the particles and continuum row of atoms is the minimum required to keep the ions in the channel. Particles approaching the row at angles larger than this will no longer undergo the gentle steering and small-angle scattering events. Rather, they will undergo large angle deflection which

will result in the particles being knocked-off the channel direction. Another measure of the channelling effect is the so called minimum yield:

$$\chi_{\min} = \frac{H_A}{H} \tag{4.23}$$

It is given by the height ratio of the aligned, H_A, to the random yield, H, for some small energy window. In practice rather than using the critical angle directly, the so called half-width angle is used instead:

$$\psi_{1/2} = C\psi_c \tag{4.24}$$

It is defined as the angle at which the backscattered yield is halfway between the minimum yield and the random yield. This half angle can be obtained through extensive calculations, [Bar71], and also through experiment by setting up a beam angular profile, figure 4.8 below:

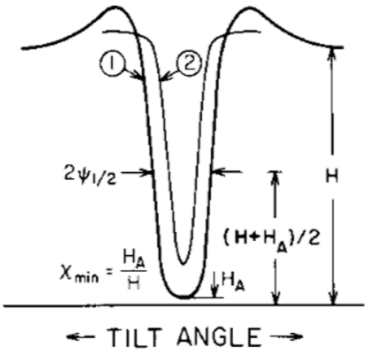

Figure 4.8: The angular beam profile showing the half-width angle and the minimum yield of a single crystal. The number 1 points to the angular profile obtained near the surface, while number 2 was obtained inside the material. Taken from reference [Chu78].

The angular beam profile is generated by tilting the sample with respect to the incident beam. It is clearly evident from this that slight deviations from the critical and half-width angle lead to substantial increases in the backscattered yield. The maximum yield in the angular profile occurs for angles slightly larger than the half-angle. The half-angle generated from the near surface region is larger than that

generated from the deep inside the crystal – in figure 4.8 this corresponds to the points 1 and 2, respectively.

Under channelling conditions the aligned component of the beam can interact with the disordered region of the crystal through wide-angle backscattering events, and also through small-angle forward scattering events. The wide-angle scattering events lead to the direct backscattering of the particles, and the small-angle forward scattering collisions lead to the deflection of the channelled particles through angles greater than the critical angle. This process is called de-channelling, and it contributes in the increase of the aligned yield. Thus, the understanding of de-channelling as a process is crucial in evaluating any damage which might exist in a crystal, or in general the crystalline nature of the sample. De-channelling can also be used to determine the number of displaced atoms from the lattice position, even the positions of impurities inside a crystalline material [Car76][Chu78][Wan09].

Damage to a crystal involves displaced atoms, strains to lattice rows, point defects, amorphous regions etc. Displaced atoms can affect channelling in two ways: Through gradual deflection of the beam particles out of channels, and through direct backscattering of the beam particles. The two types of processes can be separated into distortion type defects and obstruction type defects. Distortion type defects are mostly responsible for de-channelling as they involve small displacement of target atoms into the channels. Obstruction type defects are responsible for the direct backscattering of the beam particles, these involve amorphous regions. Lattice vibrations can be treated as another example of distortion type defect.

When a well collimated beam of particles traverses an amorphous film scattering events within the film cause the beam to spread, figure 4.9. If the film is thick enough the particles will experience a sufficient number of forward scattering collisions thereby being deflected off their initial channelled path. Consequently, if an amorphous thin film is deposited on a single crystal with an axial angle $\psi_{1/2}$, there will be an increase in the number of backscattered particles. This is because of the increased number particles that are forward scattered in the amorphous layer through angles greater than the axial half angle.

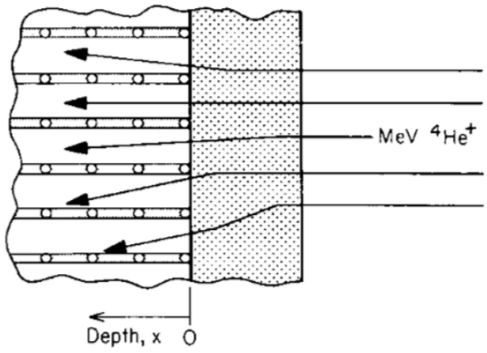

Figure 4.9: Illustration of a beam of MeV He-ions approaching a sample that has an amorphous layer deposited on a single crystal. The picture also shows the divergence of the beam due the forward scattering events with the amorphous layer. Taken from reference [Chu78].

The typical spectra that results from the particles that impinge on the layer similar to that in figure 4.9 is shown in figure 4.10 below. From this it is seen that the region which is amorphous coincides with the random spectrum. The angular yield profile of the single crystal without the amorphous film is shown with the dashed line, and that of the single crystal with the amorphous layer is shown with the solid line. It can be seen from the axial angular profiles that the minimum yield increases in the case of the amorphous layer. Another point of note concerns the half angle of the solid line clearly the half width is wider in than in the dashed line angular profile. The reason for this is that as the crystal is tilted, the particles which would in the single crystal case be de-channelled, are now deflected into the channels by the forward scattering collisions in the amorphous region.

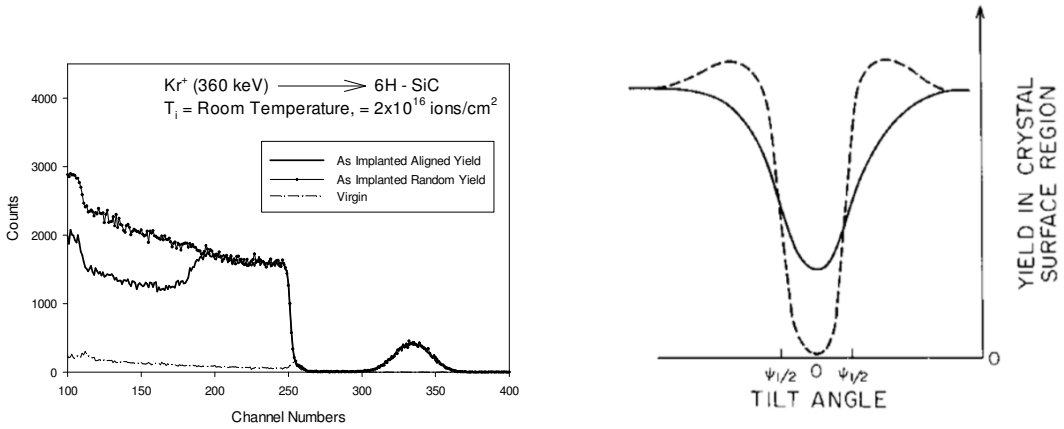

Figure 4.10: The figure on the left is a typical RBS spectra obtained from a single crystal (6H –SiC) which has an amorphous layer (As implanted aligned), and without an amorphous layer (Virgin). The figure on the right shows a typical the angular yield profiles for the single crystal without an amorphous film (Dashed line), and for the single crystal with an amorphous film (Solid line) – Angular profile taken from reference [Chu78].

A similar analysis can be applied to the case where the single crystal is damaged but not amorphous, figure 4.11. There is an increase in the backscattering yield in the damaged region. It is further noted that the yield also increases at points after the damaged region. The reason for this is that the projectile ions get de-channelled as they traverse the damaged region.

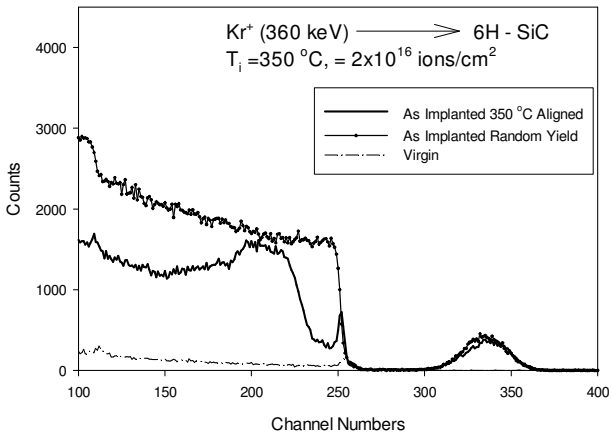

Figure 4.11: An RBS presentation of a sample which is not amorphous but has a damaged layer at some depth x from the surface.

In certain instances the material might not have an amorphous layer it may be in a polycrystalline state, however, the RBS analysis of a polycrystalline layer with highly random crystallites is similar to that of an amorphous layer. The aligned yield decreases in the case of highly oriented polycrystallites with respect to the substrate. All this is shown in figure 4.12, below.

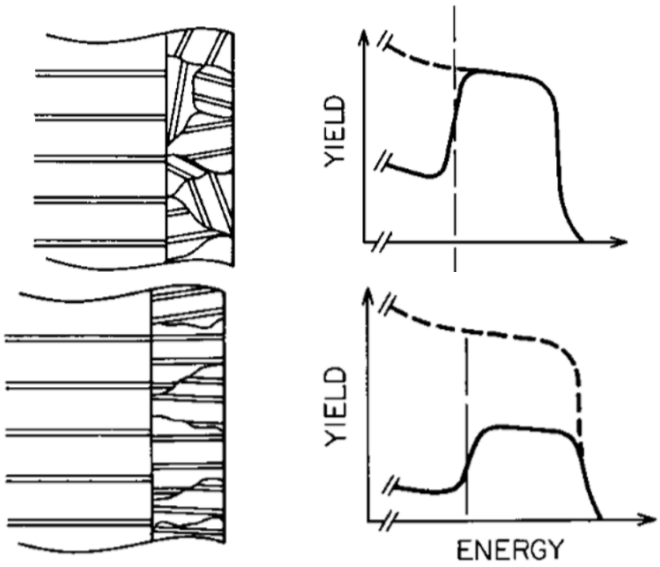

Figure 4.12: Schematic diagrams of polycrystalline layers with highly random polycrystallites (above), and one with highly oriented polycrystallites (below). Also shows are the corresponding spectra, aligned (solid lines) and random (dashed lines) – Taken from reference [Chu78].

4.5 REFERENCES

[Lin65] J. Lindhard, Mat. Fys. Medd. Dan. Vid. Selsk. **34** (1965) (14), 1.

[Bar71] J.H. Barrett, Phys. Rev. **B3** (1971) 1527.

[Dea73] G. Dearnerly, J.H. Freeman, R.S. Nelson, and J. Stephen, (1973). "Ion Implantation." North Holand Publ., Amsterdam.

[Fen73] J.S. Feng, W.K. Chu, M.-A. Nicolet, and J.W. Mayer, Thin Solid Films **19** (1973) 195.

[Car76] G. Carter, W.A. Grant, (1976). "Ion Implantation", Edward Arnold (Publishers), London.

[Chu78] W.K. Chu, J.W. Mayer, M.A. and Nicolet, (1978). "Backscattering Spectrometry." Academic Press, New York.

[Tes95] J.R. Tesmer, and M. Nastasi, (Eds). (1995). "Handbook of Modern Ion Beam Analysis." Materials Research Society, Pittsburg, Pennsylvania.

[Wa09] Y. Wang, and M. Nastasi, (Eds). (2009). "Handbook of Modern Ion Beam Analysis." Materials Research Society, Pittsburg, Pennsylvania.

[Hla10] T.T. Hlatshwayo, (2010). Ph.D. Thesis, University of Pretoria.

[www1] http://users.ictp.it/~pub_off/lectures/lns022/Mayer_1/Mayer_1.pdf - 2013 - 07 -13.

[www2] http://web.mit.edu/8.13/www/JLExperiments/JLExp15.pdf - 2013-07-13.

CHAPTER 5 EXPERIMENTAL METHOD

5.1 SAMPLE PREPARATION AND KRYPTON (Kr^+) IMPLANTATION

The starting material for this study was a 0.3 mm thick 6H-SiC wafer from Cree Research Inc. , polished on both sides with a diameter of 50 mm. Prior to implantation the wafer was cut into two and subjected to a sequence of ultrasonic agitations in acetone, de-ionised water and ultimately ethanol for about five minutes per agitation. The cleaning process was necessary for the removal of surface contamination and for degreasing the wafer. The ions were then implanted into 6H-SiC at three different temperatures, i.e. room temperature (RT), 350 ^oC and 600 ^oC. The implantations were done at the Institut für Festkörperphysik, Friedrich-Schiller-Universität, Jena, Germany. The implantation was done with 360 keV Kr ions at a fluence of 2×10^{16} ions/cm^2. The ion implantation angle was offset by 7 ^{o} with respect to the normal so as to avoid the channelling effect. An average vacuum of 10^{-4} Pa was maintained during the implantation. The ion flux was kept below 10^{13} ions/cm^2s to prevent over heating of the 6H-SiC wafer.

5.2 SAMPLE PREPARATION FOR RBS AND RBS-C MEASUREMENTS

After implantation the 6H-SiC wafer was glued onto a brass disc with Crystalbond 509^{TM}. The glue had to be heated first then smeared onto the disc. After attaching the wafer to the disc, it was allowed to cool down to allow firm contact. A Struers Accutom variable speed precision cut-off machine was used to cut the wafer into squares of approximately 5 mm in width. In order to avoid damaging the surface of the wafer, the Astruers Accutom was used at a very slow speed, complemented by spraying of water onto the cutting blade to wash-off the debris from the cutting process. As an additional precaution against physical damage a glass slide was used to cover the wafer during the cutting process. The size of the sample was intentionally

chosen to fit in the accelerator sample holder, and also for the samples to be able to accommodate a maximum collimated beam size of approximately 2mm^2. After the cutting process the samples were boiled in acetone repeatedly for approximately 4 minutes per boiling cycle. After boiling, the samples were then washed in MA 02 soap, and further rinsed in de-ionised water. Finally, the samples were soaked in methanol to remove the access water.

5.3 ANNEALING OF THE SAMPLES

Except for the as implanted RBS and RBS-C measurements, all other RBS and RBS-C measurements were preceded by an annealing cycle. The Kr implanted SiC samples were isochronally annealed in the temperature range 1000 – 1500 ^{o}C in steps of 100 ^{o}C, each cycle was performed for 5 hours. The samples were annealed in vacuum using a computer controlled Webb 77 graphite furnace. The temperature of the furnace is controlled by a Eurotherm 2704 controller connected to a pyrometer and thermocouple. The thermocouple measures all annealing temperatures below 1475 ^{o}C, whilst the pyrometer is used to measure temperatures above 1525 ^{o}C. For temperature values between 1475 and 1525 ^{o}C an average of the values recorded by both the pyrometer and the thermocouple is used. Thus, for this project the annealing temperatures from 1000 – 1400 ^{o}C were recorded by the pyrometer whilst the 1500 ^{o}C anneal was an average of the values recorded by the both the pyrometer and thermocouple. The SiC samples were placed in graphite crucibles prior to insertion into the furnace. This was necessary in order to prevent contamination of the samples by any of the gasses which might be released into the oven during the degassing process.

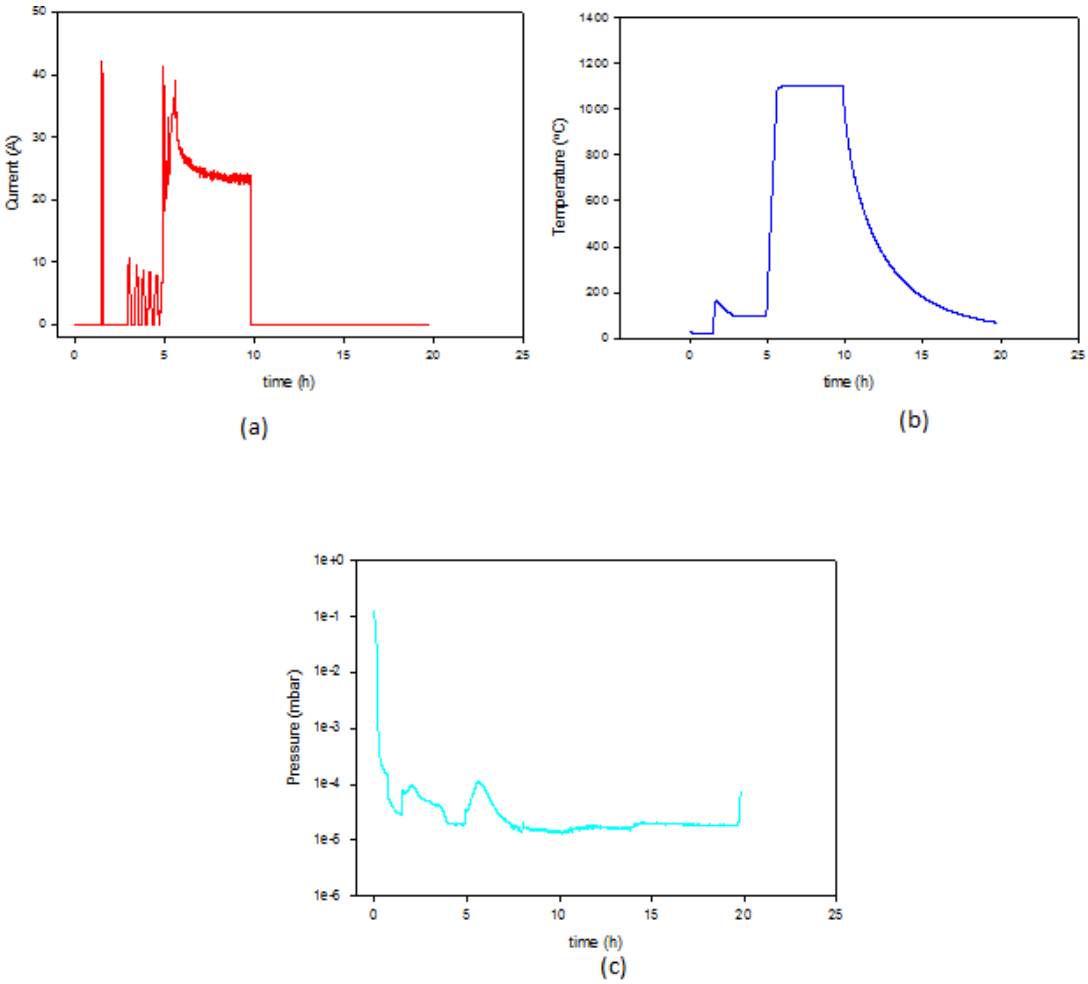

Figure 5.1: Typical Webb 77 furnace curves obtained after an annealing cycle: a) Current as a function of time, b) Temperature as a function of time, and c) Pressure as a function of time.

The crucibles containing the SiC samples were then placed inside the oven, subsequently the system was evacuated to a pressure in the 10^{-5} mbar range – this can be seen from the pressure against time curve in figure 5.1 (c). When the pressure was around the desired range the current filament was turned on – figure 5.1 (a), the temperature of the system was raised to 100 ^{o}C. This pre-annealing step was done for degassing purposes. Degassing is important to avoid huge pressure spikes during the actual annealing of the sample as a result of quantities of gas that might evolve from the inner-surfaces of the system. At the point when the temperature of the system increased the pressure in the system was also raised, as shown in figure 5.1 (c). This was a consequence of the evolution of quantities of the gas from the inner surfaces of the system, the pressure dropped as the additional gas inside the system was evacuated by the pumping system. The degassing process was carried out for about

2.5 - 3 hours. After which the current magnitude spiked before the regulatory system kicked in and the current dropped to a constant for the duration of the annealing cycle. The temperature of the system was raised to the required value for the particular annealing cycle. As expected the increase in temperature was accompanied by a rise in the pressure in the system – At every point when the temperature rises, the pressure also rises as a consequence of the evolution of gasses from the surface of the chamber. The temperature was kept at a constant value for the duration of the 5 hours annealing cycle. The pressure also decreased accordingly during this process as the pumping system was evacuating the additional gas in the system caused by the temperature increase. After the 5 hours of annealing the temperature was cooled down to a temperature just below 40 ^{o}C, at which point argon gas was pumped into the system. The cooling down was done at a much smoother manner as compared to the abrupt manner with which it was increased. The sample was then removed from the furnace and, the system flooded with additional argon gas to minimise the level of adsorption by the walls of the vessel.

As the main technique for data analysis, the operational principle of the RBS techniques is discussed next, from the production of a collimated beam of energetic particles to the data analysis.

5.4 PRODUCTION OF A COLLIMATED BEAM OF MONO-ENERGETIC IONS

5.4.1 ACCELERATOR

To generate energetic He-ions an ion source is required and to accelerate them an accelerator is needed. The accelerator that was used for this dissertation study is the University of Pretoria's Van der Graff accelerator with a maximum voltage of 2.7MeV.

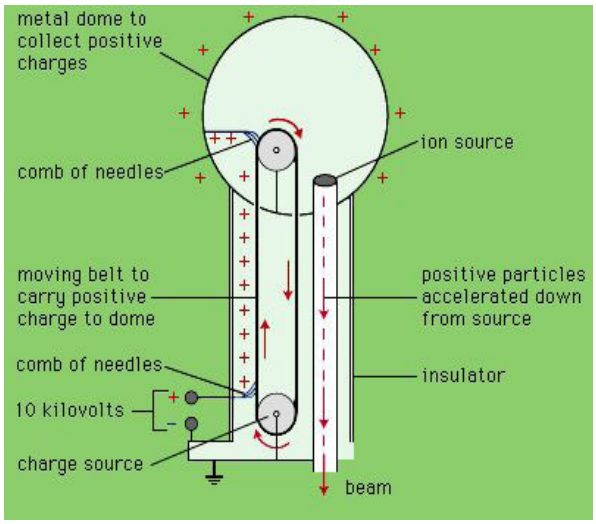

Figure 5.2: A typical schematic diagram of the Van der Graff accelerator. Figure taken from reference [www1].

A schematic diagram of the Van de Graaf accelerator is shown in figure 5.2. It consists of an insulator belt, a charge source, a metallic dome, an accelerator tube and a comb of needles at the bottom and at the top. The charge source generates charge via the triboelectric effect as the belt rotates. The bottom needles are biased such that they attract electrons from the rotating belt and aid in making the belt move up with an excess of poisitive charge. This positive charge is removed by the interaction of the belt and the comb of needles at the top. The now positively charged needles attract electrons from the metallic dome to maintain the charge neutrality, which further causes the metallic dome to remain positively charged. This process carries on for as long as it takes to set up the required voltage for a particular experiment. For the experiments of this study a maximum voltage of 1.6 MeV was used. The above mentioned process has to take place under dry conditions since humid air can interfere with the voltage build up.

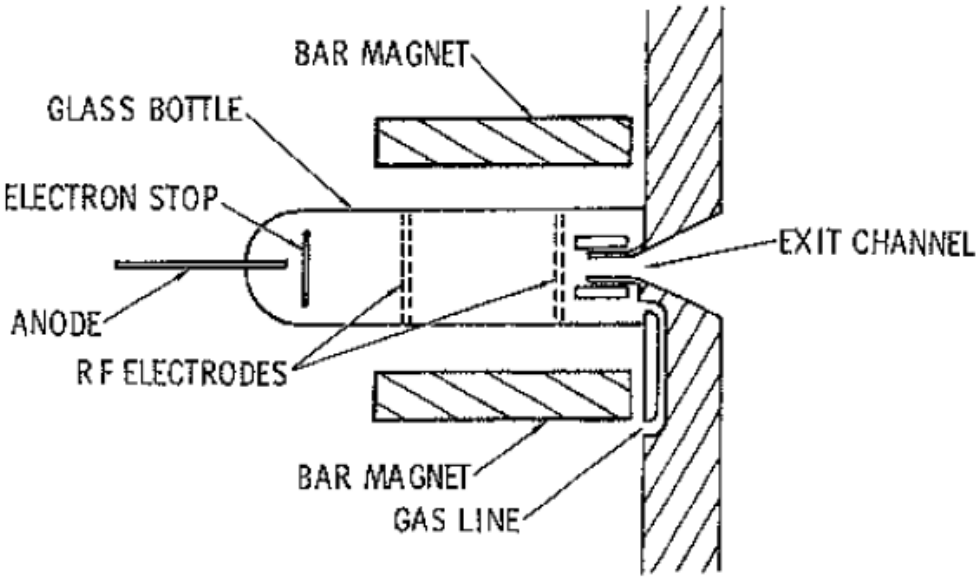

Figure 5.3: A schematic diagram of a radio-frequency ion source. Diagram taken from reference [Chu78].

5.4.2 ION SOURCE

Once the desired voltage is obtained, a gas is introduced into a glass bottle which is located inside the metallic dome. Figure 5.3 above shows a schematic diagram of a typical radio-frequency (RF) ion source. As can be seen from the figure the gas enters the glass bottle through a gas line. Inside the bottle there are two RF electrodes which produce a signal to ionise the gas as it arrives. Also found inside the glass bottle is an anode which attracts the negative charges of the plasma and repels the positive charges. Following repulsion, the positive charges are further channeled to the exit canal by application of a magnetic field. As the positive charges exit they intercept the high voltage of the dome and are forced to accelerate down the accelerator tube.

5.4.3 ANALYSING MAGNET

As the positively charged ions accelerate down the tube they constitute a “straight” beam. The particles that form the beam do not all possess the same energy and the beam itself might not be composed of one species. In addition to the Van de Graff

accelerator for beam production, the experimental set-up also includes an analysing magnet, figure 5.4 . The purpose of the analysing magnet is to act as a mass and energy selector as the beam approaches from the accelerator. By application of a magnetic field the initially “straight” beam is then bent, only those particles with the required combination of energy and mass are able to bend at the required angle and pass through the narrow slits associated with analysing magnet. Particles that have a different energy and different mass will either be bent too much or too little, thus will hit the either the low or high energy slits. Mostly it is particles with the correct combination of mass and energy that will pass through the narrow slits. The analysing magnet slits are water cooled since they intercept a large amount of beam current, and might heat-up.

5.4.4 TERMINAL POTENTIAL STABILISATION

Although the desired mass and energy of the constituent ions of the beams can be selected using the analysing magnet, fluctuations of the terminal voltage often occur during operation. This might be due to changes in the belt charging processes. As a rough estimate of the terminal voltage a generating voltmeter (GVM) is used. The GVM generates within its circuit a voltage that is proportional to the terminal voltage. A better and reliable method used for detecting the terminal voltage is that of current sensing elements refered to as high and low energy slits placed after the analysing magnet, also shown in figure 5.4. When the terminal voltage changes, the deflection of the beam by the magnet changes. If the change results in an increase of the voltage a high beam current will register on the high energy slit, and if the voltage decreases a high beam current will register on the low energy slit. The varying voltage is controlled by a set of needles called corona points through a feed back loop. Everytime the terminal voltage deviates from the expected value an error signal is sent and the operator has to re-adjust the parameters until the terminal voltage re-stabilises, this can be done by controlling the corona points. If the terminal voltage increases the corona points are moved closer to the terminal this increases the corona current and leads to a decrease in the terminal potential. In the case that the terminal voltage drops the corona points move away from the terminal, the corona current is reduced and thus leading to an increase in the terminal voltage. The beam is said to be stable or

focused if the current flowing through both slits is the same, or differs by a negligible amount. This method of potential stabilisation requires that the magnetic field be stable and that the corona points be very sharp pointed.

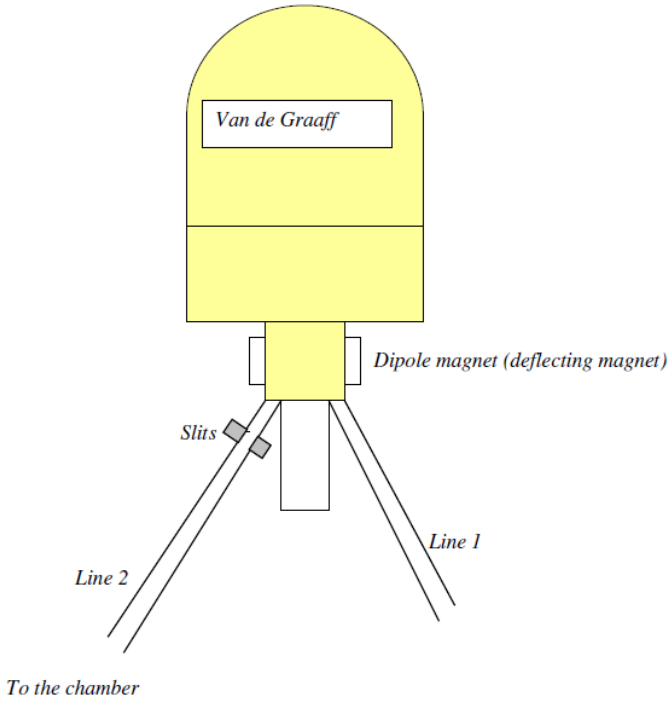

Figure 5.4: A schematic representation of the University of Pretoria's Van de Graff accelerator. Figure taken from [Hla10].

Once the beam has been focused it is transported to the chamber through a beam line. Before it reaches the chamber there is a series of vertical and horizontal slits which are used to shape and collimate the beam to a desired size. For the experiments of this project the beam size was approximately 1mm in diameter. Despite the sophistication of the beam generation and data collection (discussed below) the sample chamber is quiet simple. It is a big metallic container which houses inside it the sample holder attached to the three-axis goniometer, the detector and is connected to the vacuum system. The chamber vacuum is kept around 10^{-5} torr. This kind of vacuum is adequate for our experimental purposes and it also allows a resonable amount of time for loading and unloading of samples, which in turn allows a number of experiments to be done in a single day.

5.5 PRE-CAUTIONS

The scattering process itself only begins once the beam reaches the chamber and interacts with the sample. Since the particles are accelerated to high energies there are secondary electrons that are released from the sample which produce an additional unwanted current. This current was suppressed by a bias voltage of about -200V. Another precaution which was taken into account is pile-up. Pile-up occurs whenever the time response of the detector cannot separate between two individual events, which results in two or more separate events being recorded as a single event. This falsifies the measurements. Pile-up was prevented as well as overheating of the sample by keeping the beam current below 15nA. Additional preventive measures of pile-up are taken into consideration in the design of amplifiers. This is known as pile-up rejection [Wan09][Tes95].

During analyses one of the purposes of having a vacuum in the scattering chamber is to reduce hydrocarbon deposition onto the sample. Carbon deposition occurs if the beam is to interact with residual gases in the chamber. Also, for the purpose of increasing the pressure in the scattering chamber nitrogen gas is preferable as compared to atmospheric air to prevent the adsorption of water and carbon-dioxide to the vacuum chamber walls, which helps in increasing the pumping rate of the chamber.

5.6 DATA CAPTURING

For the detection of the backscattered particles a solid state particle detector operating with a reverse bias of -40V was used. The reverse bias is needed to create a depletion region having zero current. When the backscattered particles reach the detector they interact with the electrons transferring some of their energy to the electrons. If the electrons gain enough energy they can be able to create a current by overcoming the coulomb barrier. This then implies that the incident ions produce electron-hole pairs,

thus resulting in a current which is then integrated into a signal in the pre-amplifier Canberra 220.

The pre-amplifier is specially designed to accept a signal from the detector and with its internal circuitry amplifies the signal and tries to maximise the noise-to-signal ratio. The pre-amplifier tries to shape the detector signal, but it only achieves to form a tail pulse. The information about the radiation is encoded into the height of the processed signal.

The tail pulse from the pre-amplifier is received in the neighbouring Tennelec TC 243 amplifier, which further manipulates the signal to give a nearly Gaussian shape, and proportional in height to the output pulse of the pre-amplifier. The shaping of the signal pulse is important because it improves the resolution by reducing pile-up and it also enhances the signal to noise ratio.

A bipolar output signal from the amplifier is sent to the digital oscilloscope to monitor the shape of the output pulse, while a unipolar signal is sent to the multichannel analyser (MCA). For normal RBS data collection the pulse height analyser (PHA) mode in the MCA is used. Essentially, in the PHA each incoming pulse is sorted according to its height and placed in a certain channel address. So that any two/more pulses with the same height should be found in the same address. This results in a spectrum of frequency distributions of the heights of the incoming pulses. Each pulse which is recorded in a channel address is called a count. A normal backscattering experiment has about 512 channels. While the PHA is sorting the data, the current collected from the target sample is sent into an Ortec 439 current integrator where it is digitised. A logic signal is further sent from the current integrator into a charge counter which relays the output to the MCA and the counter. It is this logic signal which controls the starting and stopping of processing the unipolar signal from the amplifier in addition to this the logic signal instructs the counter when to start and when to stop counting.

The MCA also contains a single channel analyser (SCA) mode. The SCA is mostly used for channelling experiments. It is used to specifically select a particular energy

window for additional processing or more detailed analysis. This can be achieved by adjusting the lower and upper energy discriminators.

Whether in the PHA or SCA mode the output of the MCA is stored in a computer and consists of backscattering yield, the number of counts; and channel number(s), the addresses of the counts.

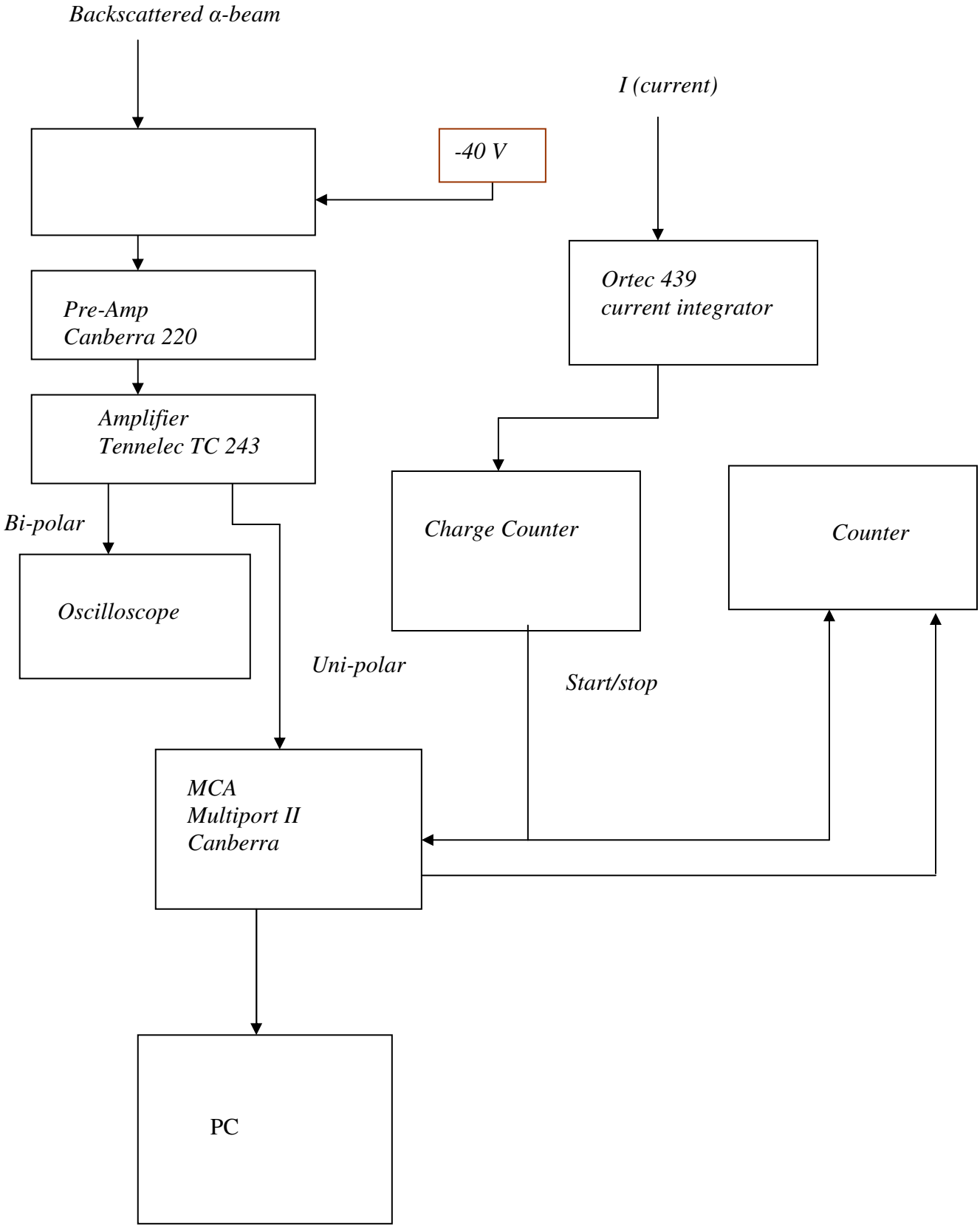

Figure 5.5: Schematic representation of the data capturing system for the RBS/ RBS – C experiments.

5.7 DATA ANALYSIS

Rutherford Backscattering Spectroscopy (RBS) was used to obtained data from the Kr implanted 6H-SiC before and after the heat treatments. After each annealing cycle the sample was taken for analysis with RBS and RBS – C. The data obtained directly from RBS was given as counts vs. channels, where the channels are linearly related to the energy of the detected particles. Thus, it was imperative to obtain the energy per channel in order to convert the energy spectrum into a depth spectrum as per discussion on depth scaling in chapter 4. The energy per channel was obtained by taking the RBS spectrum of the SiC at two different energies, i.e. 1646 keV and 1439 keV, this was then used with the known Si surface channels at these energies to obtain the energy calibration of the system. The energy calibration was later used in the STOP2 code [Fri09], which uses an algorithm similar to that discussed in the section on depth scaling in chapter 4. The code uses the energy loss data in Ziegler, [Zie77], for energy-to-depth conversions. To obtain statistical information about the implantation profiles before and after each annealing cycle the GENPLOT code was used to fit the data. The four moments which were obtained from such fit include the projected range (R_p), the projected range straggling (ΔR_p), skewness (γ), and the kurtosis (β). The data fitting was done with an Edgeworth distribution function:

$$f(x) = g(x)\,p(x)$$

where,

$$g(x) = \frac{h}{\sqrt{2\pi}} \exp\left(-\frac{\arg(x)^2}{2}\right)$$

and

$$p(x) = 1 + \frac{\gamma \cdot (\arg(x)^3 - 3\arg(x))}{6} + \frac{(\beta - 3) \cdot (\arg(x)^4 - 6\arg(x)^2 + 3)}{24}$$

with

$$\arg(x) = \frac{(x - R_p)}{\Delta R_p}$$

In the above formulation h is the height (amplitude) of the fitting curve. Since the profiles that were obtained through RBS are not exactly Gaussian, therefore the

Edgeworth was a logical fit. The assessment of diffusion by the model described in Chapter 2 requires the square of the full width at maximum, $(FWHM)^2$. The FWHM can be obtained from the projected range straggling according to:

$$FWHW = 2\Delta R_p \cdot \sqrt{2 \cdot \ln(2)}$$

The amount of Kr ions retained after each annealing cycle was also evaluated in the project. This was done by summing over the Kr depth distribution profiles for the as-implanted, and all the annealing temperatures. To assess the relative concentration of Kr ions remaining after an annealing cycle, the ratio of the sum of the Kr ions at that temperature to that of the as-implanted was used.

5.8 REFERENCES

[Chu78] W.K. Chu, J.W. Mayer, and M.A. Nicolet, (1978). "Backscattering Spectrometry.", Academic Press, New York.

[Fri09] E. Friedland, (2009). STOP2, Private communication, Department of Physics, University of Pretoria.

[Hla10] T.T Hlatshwayo, (2010). PhD Thesis, University of Pretoria, Physics Department.

[Tes95] J.R. Tesmer, and M. Nastasi, (Eds). (1995). "Handbook of Modern Ion Beam Analysis.", Materials Research Society, Pittsburg, Pennsylvania.

[Wa09] Y. Wang, and M. Nastasi, (Eds). (2009). "Handbook of Modern Ion Beam Analysis.", Materials Research Society, Pittsburg, Pennsylvania.

[www1] http://www.britannica.com/EBchecked/media/59675/Schematic-diagram-of-a-Van-de-Graaff-high-voltage-electrostatic. 13/10/11.

[Zie77] J.F. Ziegler, (1977). "The Stopping and Range of ions in Matter.", Pergamon Press, New York.

CHAPTER 6 RESULTS AND DISCUSSION

The recovery of lattice damage and diffusion of implanted Krypton (Kr) in 6H-SiC were investigated by Rutherford backscattering spectrometry (RBS) and Rutherford backscattering combined with channelling (RBS-C). The damage in the single 6H-SiC was introduced by implantation of 360 keV Kr ions up to a fluence of 2×10^{16} ions/cm^2. The Kr ions were implanted at room temperature (RT), 350 °C and 600 ^{o}C. The thermal annealing was done isochronally in vacuum, using the Webb 77 furnace, in the temperature range 1000 – 1500 ^{o}C in steps of 100 ^{o}C, for 5 hours. This chapter presents and discusses the results of this study in three sections: Section 6.1 is based on the ion implantation effects at the different temperatures; Section 6.2 focuses on the results obtained from the room temperature implantation and finally the results of high temperature implantations (350 and 600 ^{o}C) are presented and discussed in section 6.3.

6.1 ION IMPLANTATION

Figure 6.1 shows RBS and RBS-C results of 6H-SiC implanted with Kr ions at the different implantation temperatures (Room Temperature (RT), 350 ^{o}C, and 600 ^{o}C). An aligned spectrum obtained from a virgin sample (un-implanted 6H-SiC) is included for comparison as it defines the lower level limit of the backscattering spectra. The random spectrum is also included for comparison as it is used to define the upper level limit of the backscattering spectra. Implantation of Kr-ions into 6H-SiC at RT caused an amorphous layer to a depth of approximately 280 nm from the surface. This is indicated by the overlap of the RT aligned spectrum and the random spectrum to a depth of approximately 280 nm. The overlap occurred because there was no channelling in the amorphous layer. Therefore, the same amount of backscattered He^{-}ions from the atoms in the amorphous layer and in the random direction of the crystal was detected.

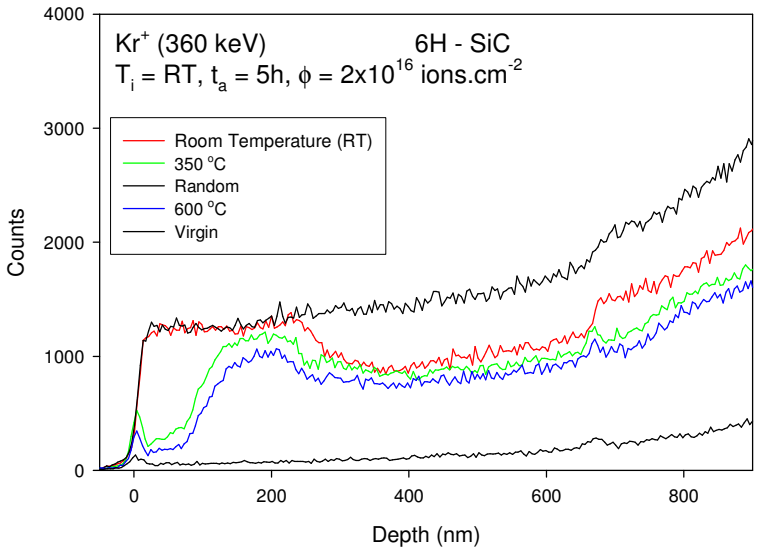

Figure 6.1: RBS and RBS-C spectra of 1.4 MeV He ions backscattered on 6H-SiC which was implanted with 360 keV Kr ions at three different temperatures (RT, 350 °C and 600 °C) up to a fluence of 2×10^{16} ions/cm^2. An un-implanted spectrum is included for comparison.

Implantations at 350 and 600 °C did not amorphise the 6H-SiC. The crystalline 6H-SiC retained defects, and/or defect clusters. The defects retained in the 6H-SiC are represented by the broad peaks around 200 nm. The damage peak is usually a consequence of direct backscattering from the displaced atoms (in our case Si atoms). The defects retained (consequently the aligned yield) after 350 °C implantation are more than defects retained after 600 °C implantation. Nonetheless, in both implantations the 6H-SiC was not amorphised. This could imply that these implantation temperatures are above the critical temperature at which 6H-SiC can be amorphised. A critical temperature for amorphisation is the temperature above which amorphisation does not occur. During the implantation process there is a competition between damage production, and annealing of this damage [Web12][Wen98]. The damage production can be described according to various models [Hec86][Wen98][Web00]. The dynamic annealing of the radiation damage can be described according to the Morehead and Crowder model [Mor72], and other models [Web94a][Web94b][Jac88]. The scope of this project was not large enough to establish which model in particular was relevant for the damage production, and the recovery processes. Amorphisation, in general, occurs when the rate of damage production exceeds the rate of the recovery processes. The latter seems to be the case for the room temperature implantation. From figure 6.1, it is clear that at 350 and

600 °C the rate of recovery exceeds the rate of damage production, and the 6H-SiC retains its crystalline structure although it still contains some damage. Using only RBS it is difficult to specify the types of defects retained after high temperature implantation. However, it is clear that the damage retained in the RT implantation and the higher temperature implantations are different. According to Wesch et al., [Wes95a][Wes95b], the damage retained by high temperature implantation is influenced by defect recombination, diffusion and transformation during implantation. The overall observation from these results is that a higher implantation temperature reduces the radiation damage retained in 6H-SiC.

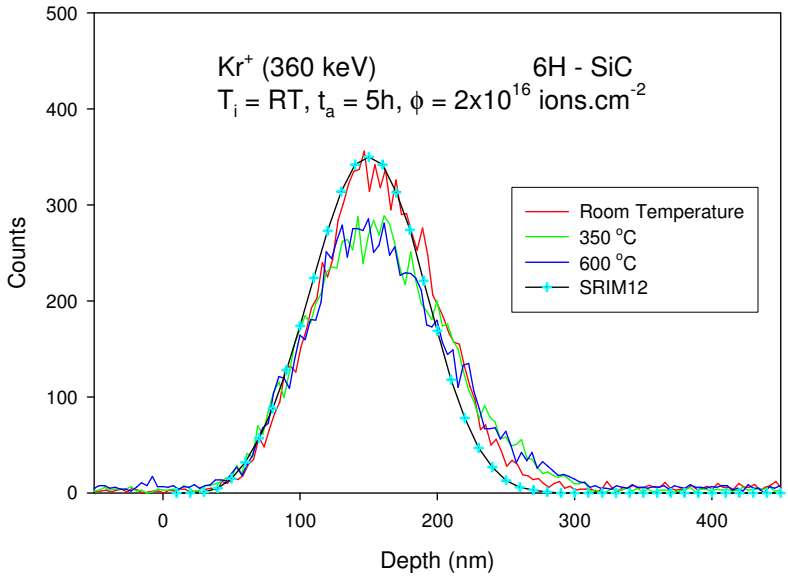

Figure 6.2: The depth profiles of Kr implanted into 6H-SiC at RT, 350 °C, and 600 °C as compared to SRIM 2012 simulation [www1].

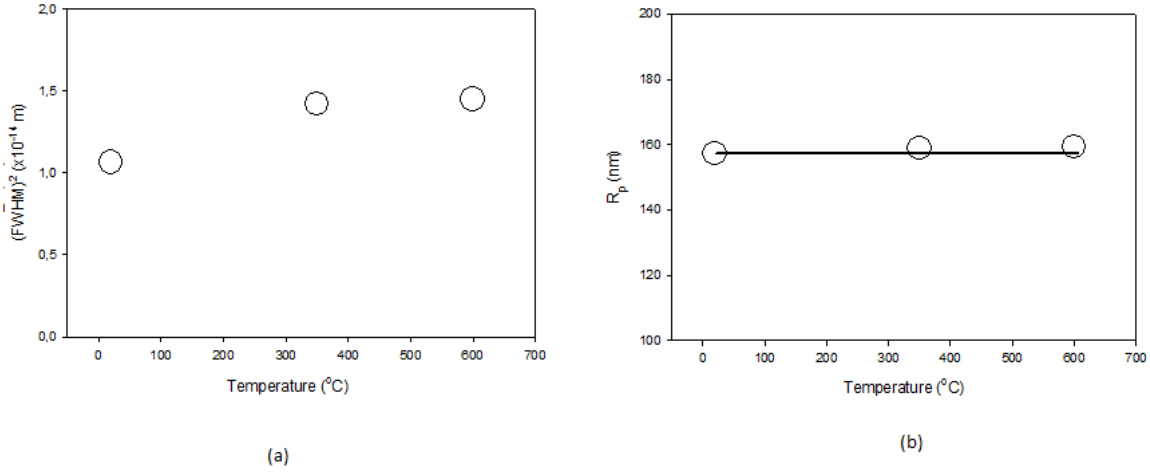

Figure 6.3: (a) The square of the full width at half maximum, $(FWHM)^2$ and, (b) the projected ranges(R_p) of the Kr depth profiles as a function of implantation temperature.

The depth profiles of Kr implanted into 6H-SiC at RT, 350 °C, and 600 °C as compared with SRIM 2012 simulation [www1] are shown in figure 6.2. The results obtained from the SRIM simulation correspond very well with the experimental data for the room temperature implantation. The deviation from the high temperature implantation result was expected in accordance with the assumptions that the SRIM program uses, see Chapter 3. The depth profiles were fitted with an Edgeworth function using the GENPLOT code to characterise their distribution. The experimental moments of the profiles and SRIM moments are shown in table 1. The implantation profiles are approximately Gaussian, the skewness ($\gamma \sim 0$) and the kurtosis ($\beta \sim 3$). Figure 6.3 shows the square of the full width at half maximum $(FWHM)^2$ and the projected range (R_p) of the as-implanted Kr profiles as functions of temperature. The FWHM is related to the range straggling, ΔR_p, through $FWHW = 2\Delta R_p \cdot \sqrt{2 \cdot \ln(2)}$. The high temperature implants have broader profiles in comparison to the room temperature implant – figure 6.3(a). This implies that during the high temperature implantations there was diffusion of the implanted Kr in the 6H-SiC. The projected ranges of all three implants are comparable – figure 6.3(b), thus there was no shift of the Kr depth distribution profile during the high temperature implantation.

Table 1: The first four moments of the Kr depth profiles obtained from fitting the Edgeworth function using the GENPLOT code, and SRIM 2012.

Temperature (^{o}C)	Projected Range, R_p, (nm)	Range Straggling, ΔR_p, (nm)	Skewness, γ	Kurtosis, β
20	157.2	43.79	0.1408	2.865
350	158.9	50.59	0.3259	2.804
600	159.3	51.16	0.4548	2.988
SRIM12	154.3	41.58	0.01280	2.752

6.2 ROOM TEMPERATURE IMPLANTATION

6.2.1 RADIATION DAMAGE

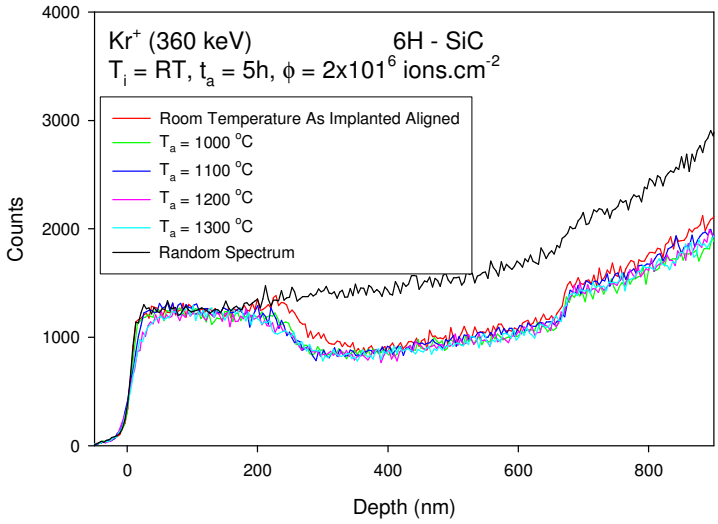

Figure 6.4: RBS and RBS-C spectra of 1.4 MeV He ions backscattered from 6H-SiC implanted with 360 keV Kr at room temperature after isochronally annealing in the temperature range 1000 – 1300 ^{o}C for 5 hours. The random and as-implanted RBS-C spectra are included for comparison.

Figure 6.4 shows a series of RBS-C spectra obtained after isochronally annealing the room temperature implanted 6H-SiC from 1000-1300 °C in steps of 100 °C for 5 hours. The random and as-implanted aligned spectra are included for comparison. Annealing at 1000 ^{o}C resulted in slight epitaxial re-crystallisation of the amorphous 6H-SiC from the amorphous-crystalline interface. This is consistent with other published results which reported that re-crystallisation of amorphous SiC starts at temperatures around 1000 ^{o}C [Wen98][Höf99][Aud07]. The RBS-C spectrum of the sample annealed at 1100 ^{o}C was basically identical to the one for the 1000 ^{o}C sample. This implies that during the first annealing cycle at 1000 ^{o}C the amorphous region annealed into a more thermally stable defect structure. Several authors have reported that the amorphous SiC region also forms polycrystalline grains at these temperatures [Hef96][Pac96a][Pac96b][Boh87]. In this study only RBS and RBS-C were used. RBS/RBS-C technique is not able to distinguish between an amorphous structure and a highly mis-oriented polycrystalline structure. Therefore, the overlapping region will still be referred to as an "amorphous layer". Annealing at 1200 ^{o}C and 1300 ^{o}C did not result in any further epitaxial growth from the amorphous-crystalline interface. A slight reduction in the RBS yield was observed on the surface region of the SiC at 1200 ^{o}C. This could be due to a statistical nucleation of grains from the upper part of the amorphous layer as proposed by Wendler et al., [Wen98].

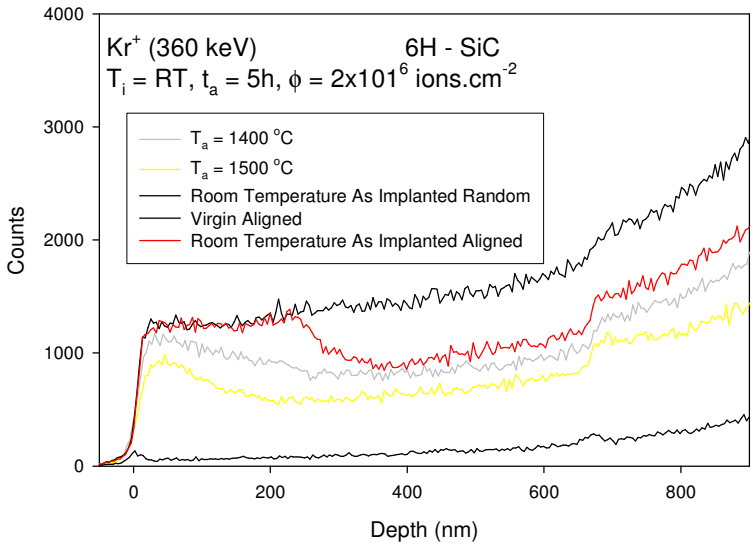

Figure 6.5: RBS and RBS-C spectra of 1.4 MeV He ions backscattered from 6H-SiC implanted with 360 keV Kr at room temperature after isochronally annealing in the temperature range 1400 – 1500 °C for 5 hours. The un-implanted and as-implanted aligned spectra are included for comparison.

Annealing at 1400 °C resulted in an extensive epitaxial re-crystallisation of the 6H-SiC as shown in figure 6.5. The re-crystallised 6H-SiC still contains a high density of defects. At 1500 °C further reduction in the damage density of the 6H-SiC occurred. The surface region is still severely damaged, and the damage exhibits a peak comparable to that of the high temperature implantations. The observed re-crystallisation behaviour in response to the isochronal annealing cycles is to a level comparable to the results obtained by Bohn et al., [Boh87]. They found that complete epitaxial re-crystallization of SiC occurred near a temperature of 1500 °C in an explosive manner. By explosive they meant that the crystallization was drastic over a narrow temperature range near 1500 °C. Wendler et al., [Wen98], also reported on the drastic re-crystallisation of implanted SiC after annealing at 1500 °C. In their discussion they attributed the sudden reduction in damage to the thermal etching of the SiC. The results of this study and those of the cited references all coincide with the recent results obtained by Hlatshwayo et al., [Hla12].

6.2.2 DIFFUSION

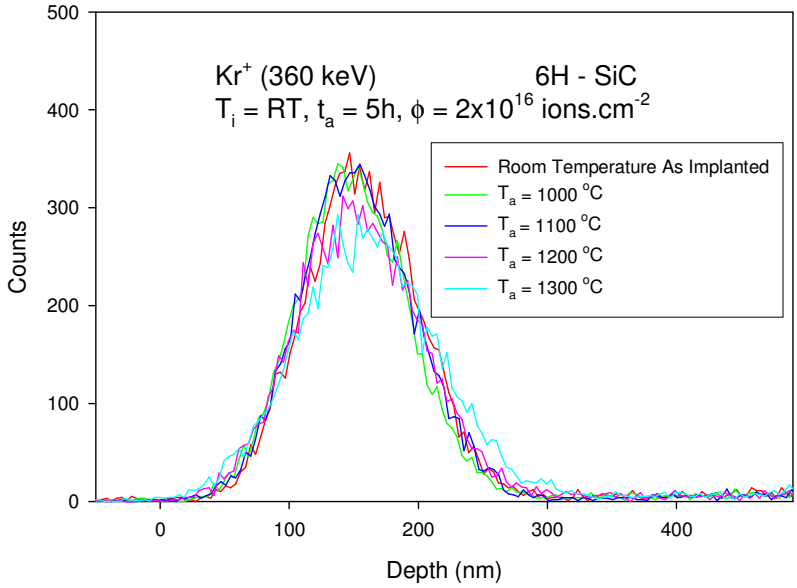

Figure 6.6: Depth distribution profiles of the Kr after isochronally annealing the implanted 6H-SiC in the temperature range 1000 – 1300 °C, in steps of 100 °C for 5 hours as compared to the as-implanted Kr depth profile.

Table 2: The first four moments of the Kr depth distribution obtained from fitting the Edgeworth function using the GENPLOT code.

Temperature (°C)	Projected Range, R_p (nm)	Range Straggling, ΔR_p (nm)	Skewness (γ)	Kurtosis (β)
20	157.2	43.79	0.1408	2.864
1000	156.7	43.39	0.1858	2.993
1100	154.2	44.20	0.2618	2.915
1200	154.8	48.41	0.1965	2.910
1300	161.2	56.18	0.1803	3.277

The Kr depth profiles for the as-implanted and isochronal annealing experiments in the temperature range 1000 – 1300 ^{o}C in steps of 100 °C are shown in figure 6.6. These profiles display a nearly Gaussian distribution as can be seen from the moments in table 2. The moments were obtained by fitting the Kr depth profiles to an Edgeworth function using the GENPLOT code. The profiles for the annealing temperature range 1400 – 1500 ^{o}C in steps of 100 °C as compared with the as-implanted profile are shown separately in figure 6.8. The distribution profiles at these high annealing temperatures seem to have assumed an asymmetric form. The diffusion model described in Chapter 2 does not apply to the distribution profiles that display an asymmetric form.

Figure 6.7 presents the supporting information pertinent to the diffusion of the room temperature implanted Kr into the 6H-SiC after annealing in the temperature range 1000 – 1300 °C. Figure 6.7(a) shows the square of the full width at half maximum $(FWHM)^2$ as a function of annealing temperature and figure 6.7(b) shows the peak position as a function of annealing temperature.

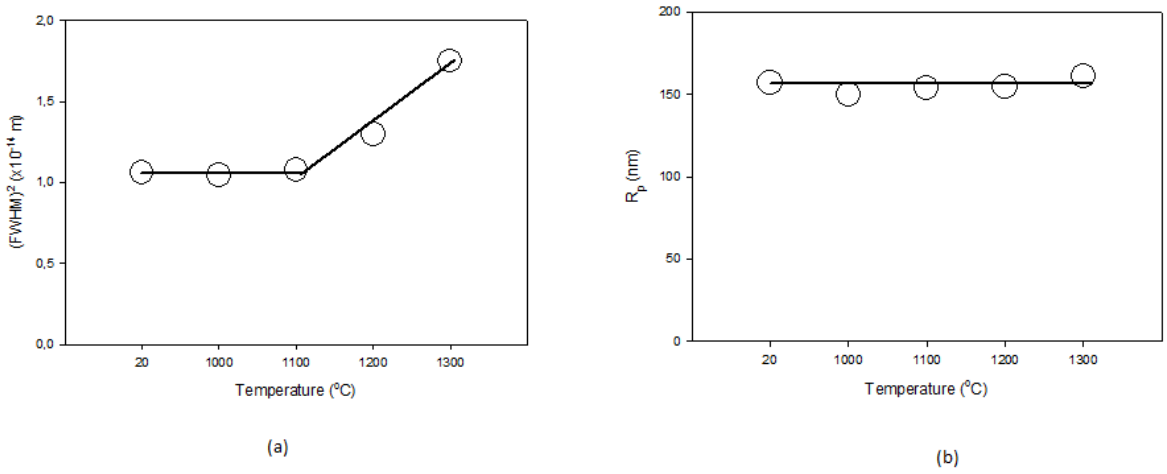

Figure 6.7: (a) The square of the full width at half maximum, $(FWHM)^2$, and the (b) peak positions of the Kr depth profiles after isochronally annealing the Kr implanted 6H-SiC in the temperature range 1000 – 1300 ^{o}C, for 5 hours in steps of 100 ^{o}C , as functions of annealing temperature.

The results in figure 6.7(a) also show that there was no broadening in the Kr depth distribution profiles after annealing at 1000 and 1100 °C. Thus, no diffusion took place at these temperatures. The broadening of the Kr depth distribution profiles

occurred after annealing at 1200 °C. This is an indication that there was a slight diffusion of the Kr within the SiC matrix at this temperature. More diffusion of the Kr in the 6H-SiC matrix was observed after annealing at 1300 °C. During the diffusion process of the Kr at 1200 and 1300 °C, the Kr depth profiles maintained their approximately Gaussian shape and there was no loss of Kr – figure 6.9. According to the diffusion model described in Chapter 2 the Kr diffusion at these annealing temperatures can be described by a Fickian type diffusion process.

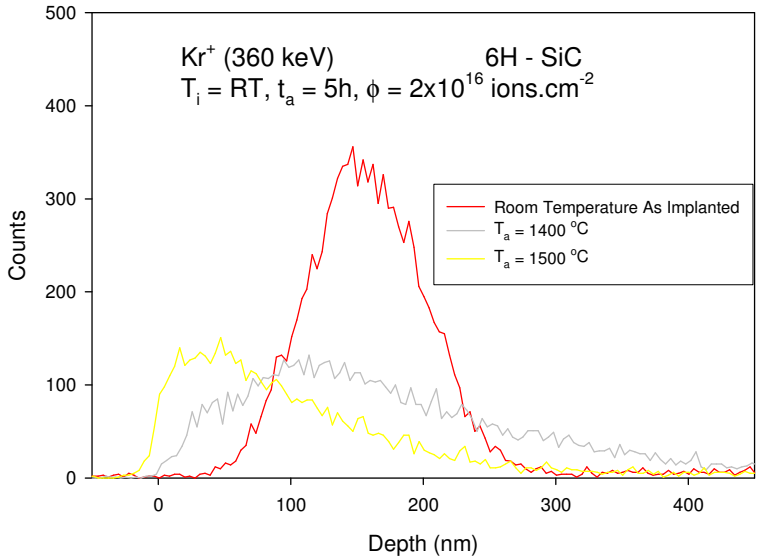

Figure 6.8: Depth distribution profiles of Kr implanted into 6H-SiC at room and submitted to isochronally annealing in the temperature range 1400 – 1500 °C, in steps of 100 °C for 5 hours. The as implanted Kr depth profile is included for comparison.

Annealing at 1400 °C resulted in a Kr transport mechanism that cannot be explained in terms of the Fickian process because of the asymmetry, as shown in figure 6.8. Annealing at this temperature caused a shift of the Kr towards the surface, and some of the Kr appears to have penetrated the bulk extending deeper into the 6H-SiC matrix. This behaviour seems to have occurred simultaneously with the extensive reduction in the damage layer of the SiC (as already discussed in the radiation damage sub-section 6.2.1). The shift of Kr towards the surface resulted in a loss of about 30% of the Kr after the annealing cycle – figure 6.9. Annealing at 1500 °C caused some

further shift of the Kr profile towards the surface - figure 6.8. This shift was accompanied by a total loss of about 50% of the Kr from the surface. The loss of Kr and sudden shift of the Kr towards the surface could be evidence of the thermal etching of the SiC surface during the annealing cycles at these temperatures as reported by Wendler et al., [Wen98]. They also observed the rapid epitaxial growth of the damaged SiC at high annealing temperatures, 1500 ^{o}C specifically. At this temperature they also reported a complete loss of the implanted ions to thermal etching. To further support the possibility of the thermal etching of the SiC the work done by van der Berg et al., [Ber10], showed that 6H-SiC thermal etching has already started at these high annealing temperatures. In a more recent study, Hlatshwayo et al., [Hla12], reported results which are in agreement with the above mentioned studies. This thermal etching could also be the reason for the sudden re-crystallisation of the SiC (discussed in sub-section 6.2.1). It may be that the damaged layer was thermally etched, leaving only the partially damaged region of the 6H-SiC. Thermal etching also results in an uneven surface. Since RBS is very sensitive to surface uniformity, it could also be that the observed diffusion towards the bulk at 1400 ^{o}C is a manifestation of the surface roughness.

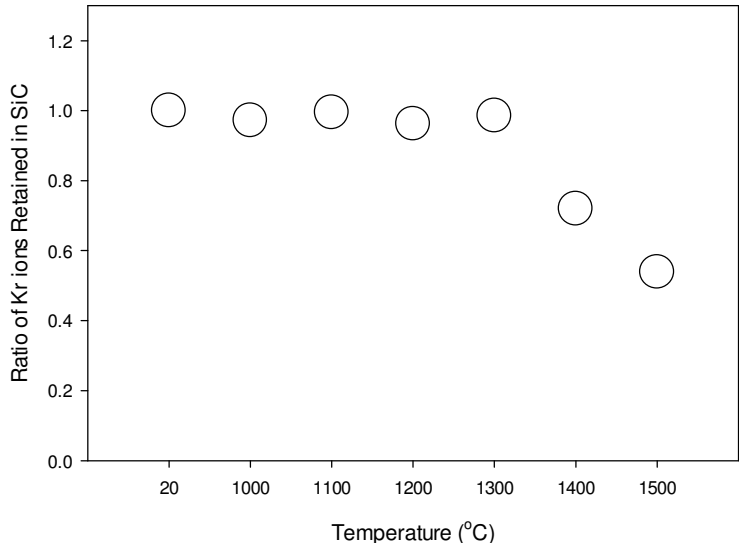

Figure 6.9: The relative ratio of the amount of Kr ions that remained inside the SiC matrix as a function of the annealing temperature.

6.3 HIGH TEMPERATURE IMPLANTATIONS

6.3.1 RADIATION DAMAGE

Figure 6.10 and 6.11 show the series of RBS-C spectra obtained after isochronally annealing the 350 and 600 ^{o}C implanted 6H-SiC samples in the temperature range 1000 – 1500 ^{o}C, in steps of 100 ^{o}C for 5 hours, respectively. The random, un-implanted (aligned) and as-implanted (aligned) spectra are included for comparison.

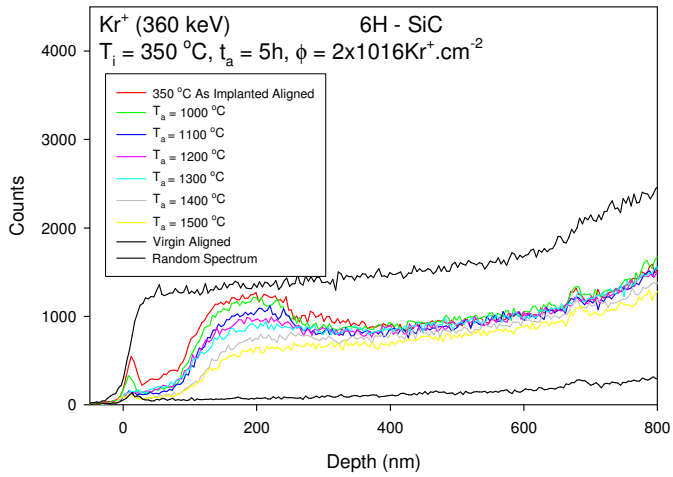

Figure 6.10: RBS and RBS-C spectra of 1.4 MeV He ions backscattered from 6H-SiC implanted with 360 keV Kr ions at 350 ^{o}C after isochronally annealing in the temperature range 1000 – 1500 ^{o}C, in steps of 100 ^{o}C for 5 hours. The random; un-implanted and as-implanted RBS-C spectra are included for comparison.

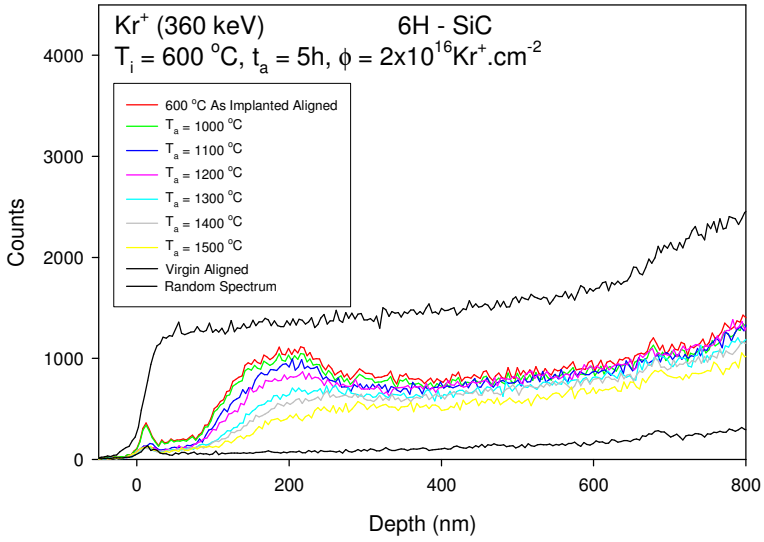

Figure 6.11: RBS and RBS-C of 1.4 MeV He ions backscattered from 6H-SiC implanted with 360 keV Kr ions at 600 °C after isochronally annealing in the temperature range 1000 – 1500 °C, in steps of 100 °C for 5 hours. The random; un-implanted and as-implanted RBS-C spectra are included for comparison.

In order to evaluate the radiation damage recovery during the annealing cycles the results in figure 6.10 and 6.11 were used to estimate the relative damage in the crystalline 6H-SiC samples. This was done by taking the ratio of the total number of counts in the damaged region to the total number of counts in the random spectrum in the same region. The region used in these calculations was from 40 nm to about 400 nm. The 40 nm was selected because it is immediately after the surface peak, and the 400 nm is the approximate depth at which the damage terminates. As can be seen from figure 6.12 each annealing cycle in the range 1000 – 1500 °C caused a decrease in the relative damage retained in the SiC samples. A decrease in the backscattering yield with each annealing cycle is observed. These results also reveal that the damage retained in the 350 °C implanted sample after annealing was always more than that in the 600 °C implanted sample. Despite the annealing of radiation damage in the temperature range of interest i.e. 1000 – 1500 °C, the damage retained after implantations could not be completely annealed out. The damage level for the un-implanted 6H-SiC is represented by the solid line in figure 6.12, and it is at approximately, 0.0566. The minimum relative damage retained after annealing the 6H-SiC samples(implanted at 350 and 600 °C) at 1500 °C was 0.370 and 0.265, respectively. From the nature of the aligned spectra around the damaged region it can

be seen that the type of defects that were retained in both SiC samples after implantation are different from the defects retained in the SiC after the 1500 ^{o}C annealing cycle. This can be inferred from the shape of the aligned spectra around the 40 nm – 400 nm damaged region. In the as-implanted spectrum there is an upward bulge which is an indication of direct backscattering from displaced atoms in this region, whereas in the 1500 ^{o}C spectrum the yield is flat indicating no localised region of direct backscattering by displaced atoms. This may suggest that the damage produced by the high temperature implantation consists of a combination of point defects and more complex defect clusters as is reported by [Hef95][Wes95a][Wes95b][Hef96]. The reduction in the localised damage peak in the temperature range 1000 – 1300 °C could further imply that many defects have annealed out. Annealing at 1500 ^{o}C caused significant reduction of the complex defects as can be seen from the consequent reduction of the backscattering yield, see figures 6.10 and 6.11. This effect is more pronounced in the 600 ^{o}C implantation, figure 6.11. The aligned spectrum (despite the reduction in the damage after annealing at 1500 ^{o}C) did not reach the level of the un-implanted spectrum. This implies that the damage retained after the implantation was not completely annealed out in the temperature range of interest. This is in contrast to the work done by Heft et al., [Hef95][Hef96], and Wendler et al., [Wen98]. The work done by these authors showed that ion implantation at 600 ^{o}C into 6H-SiC causes a huge reduction in the damage retained after annealing at 1500 ^{o}C, almost comparable to the un-implanted sample. The reason for this discrepancy can be attributed to the high fluence that was used in the present study. Wendler et al., [Wen98], also observed that implantation at a high temperature and high fluence has a negative influence on the recovery of the damaged SiC.

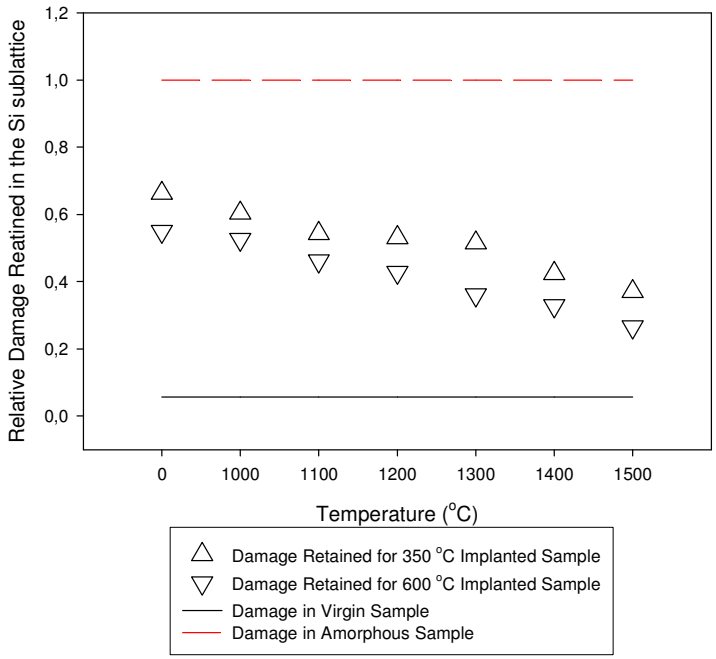

Figure 6.12: The relative radiation damage of the Kr implanted 6H-SiC in the Si sub-lattice as a function of the annealing temperature. The triangles facing up denote the 350 °C implantation results. The triangles facing down denote the 600 °C implantation results. The dashed line represents the random case corresponding to absolute damage – amorphisation. The solid line represents the lower limit corresponding to the virgin sample.

6.3.2 DIFFUSION

The Kr depth profiles after isochronal annealing the 350 and 600 °C implanted samples in the temperature range 1000 – 1500 °C in steps of 100 °C for 5 hours are shown in figure 6.13. The as implanted Kr depth profiles are included for comparison. The Kr depth profiles were fitted with an Edgeworth function using the GENPLOT code in order to characterise the diffusion behaviour of the implanted Kr with annealing temperature. Figure 6.14 shows the square of the full at half maximum $(FWHM)^2$ and peak position of the Kr profiles as functions of annealing temperature. The Kr profiles have a nearly Gaussian shape as can be seen from the moments in table 3.

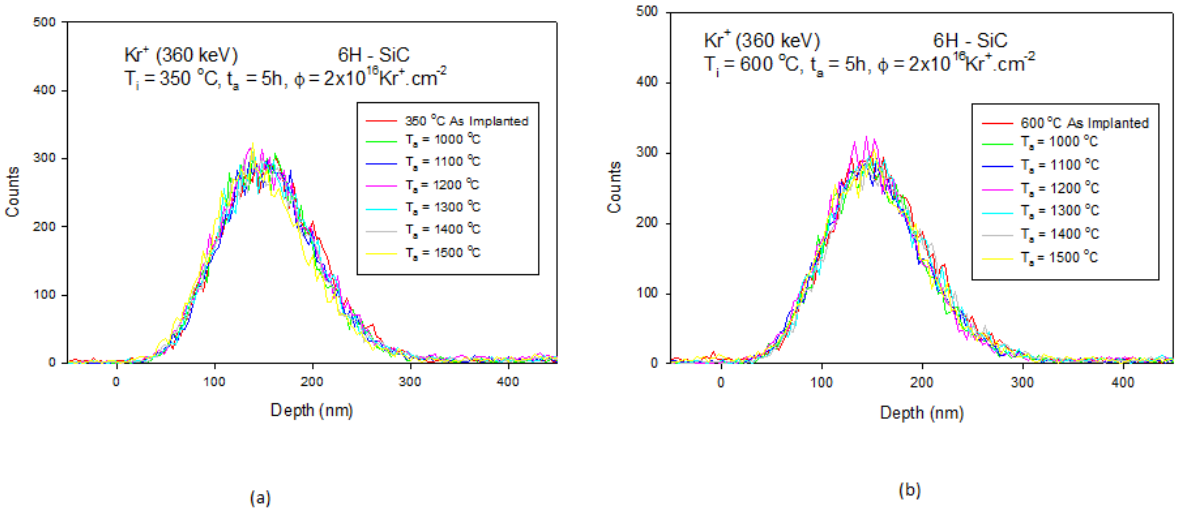

Figure 6.13: Depth distribution profiles of the Kr ions after isochronally annealing in the temperature range 1000 – 1500 °C, in steps of 100 °C for 5 hours per cycle. (a) The substrate is 6H – SiC implanted with Kr ions at 350 °C, (b) 600 °C, both, up to a fluence of 2×10^{16} ions/cm^2.

Table 3: The first four moments of the Kr depth distribution obtained from fitting the Edgeworth function using the GENPLOT code,(a) 350 °C, (b) 600 °C.

Temperature (°C)	Projected Range, R_p (nm)	Range straggling, ΔR_p (nm)	Skewness, γ	Kurtosis, β
350	158.6	50.57	0.3276	2.798
1000	155.3	49.03	0.3448	2.983
1100	155.7	49.35	0.3503	3.015
1200	156.0	51.13	0.4055	2.987
1300	155.9	49.94	0.3619	2.929
1400	155.4	50.13	0.3623	2.939
1500	149.1	49.52	0.4298	2.975

(a)

Temperature (^oC)	Projected Range, R_p (nm)	Range straggling, ΔR_p, (nm)	Skewness, γ	Kurtosis, β
600	159.3	51.09	0.4580	2.974
1000	154.9	49.72	0.3745	3.120
1100	155.1	50.38	0.4049	3.093
1200	155.2	49.46	0.3974	3.182
1300	157.9	50.35	0.4500	2.941
1400	159.9	50.94	0.4153	3.047
1500	154.8	51.70	0.4392	3.174

(b)

Figure 6.14 (a) shows that there was no change in the $(FWHM)^2$ after isochronally annealing the 350 and 600 ^oC implanted samples in the temperature range 1000 – 1500 ^oC. These results imply that there was no Kr diffusion in the 6H-SiC matrix after annealing at these temperatures. Figure 6.14 (b) shows that there was also no shift in the Kr profiles in the annealing temperature range. These results suggest that the rate of thermal etching of 6H-SiC in the high temperature implanted sample is very low in comparison to the room temperature implantation. As a result of the slow thermal etching rate there was no Kr loss from 6H-SiC surface, all the Kr was retained inside – figure 6.15.

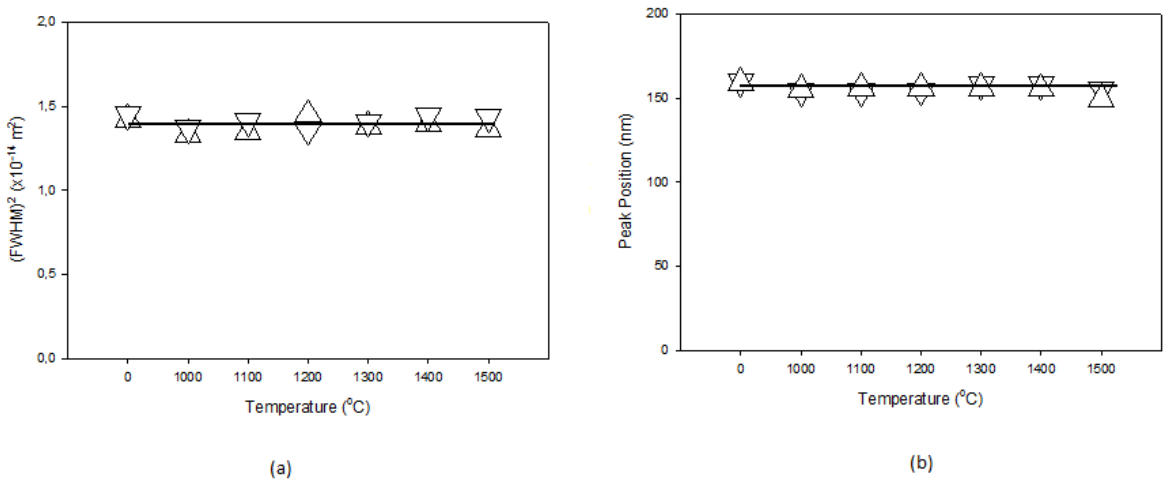

Figure 6.14: (a) The square of the full width at half maximum $(FWHM)^2$ of the Kr depth profiles as a function of the annealing temperature,(b) The peak positions of the Kr depth profiles as a function of the annealing temperature. The triangles facing up denote the 350 °C implantation results. The triangles facing down denote the 600 °C implantation results.

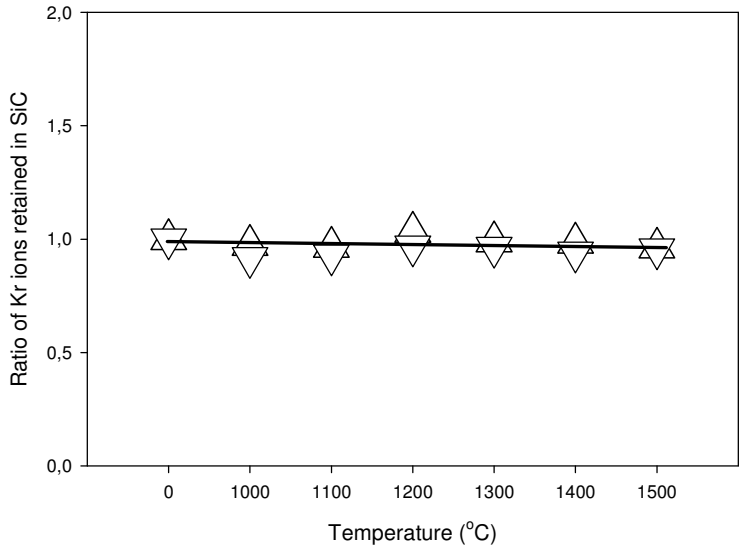

Figure 6.15: The relative ratio of the amount of Kr ions that remained inside the SiC matrix as a function of the annealing temperature. The triangles facing up denote the 350 °C implantation results. The triangles facing down denote the 600 °C implantation results.

6.4 REFERENCES

[Ber10] N. G. Van der Berg, J.B. Malherbe, A.J. Botha, E. Friedland, Surf. Interface Anal. **42** (2010) 1156.

[Boh87] H.G. Bohn, J.M. Williams, G.M. Begun, J. Mat. Res. **2** (1987) 107.

[Cal97] L. Calcagno, M.G. Grimaldi, P. Musumeci, J. Mat. Res. **12** (1997) 1727.

[Hec86] N. Hecking, K.F Heidemann and E. Te Kaat, Nucl. Instr. and Meth. **B 15** (1986) 760.

[Hef95] A. Heft, E. Wendler, T. Bachmann, E. Glaser, W. Wesch, Mat. Sci. Eng. **B 29** (1995) 142.

[Hef96] A. Heft, E. Wendler, J. Heindl, T. Bachmann, E. Glaser, H.P. Strunk, W. Wesch, Nucl. Instr. and Meth. **B 116** (1996) 239.

[Hla12] T.T. Hlatshwayo, J.B Malherbe, N.G. van der Berg, L.C. Prinsloo, A.J. Botha, E. Wendler, Nucl. Istr. and Meth. **B 274** (2012) 120.

[Höf99] A. Höfgen, V. Heera, F. Eichhorn, W. Skorupa, W. Möller, Mat. Sci. Eng. **B 61-62** (1999) 353

[Jac88] K.A. Jackson, J. Mat. Res. **3** (1988) 6.

[McH93] C.J. Mchargue, J.M. Williams, Nucl. Inst, and Meth. **B 80/81** (1993) 889.

[Mor70] F.F. Morehead, B.L. Crowder, Rad. Eff. **6** (1970) 27.

[Pac96a] Y. Pacaud, W. Skorupa, J. Stoemenos, Nucl. Instr. and Meth **B 120** (1996) 181.

[Pac96b] Y. Pacaud, J. Stoemenos, G. Brauer, R.A. Yankov, V. Heera, M. Voelskow, R. Kögler, R. Skorupa, Nucl. Instr. and Meth. **B 120** (1996) 177.

[Web94a] W.J. Weber, R.C Ewing, L.M. Wang, J. Mat. Res. **9** (1994) 688.

[Web94b]W.J. Weber, L.M. Wang, Nucl. Instr. and Meth. **B 91** (1994) 63.

[Web00] W. J. Weber, Nucl. Instr. and Meth. **B 166/167** (2000) 98.

[Web12] W.J. Weber, Y. Zhang, L.M. Wang, Nucl. Instr. and Meth. **B 277** (2012) 1.

[Wen98] E. Wendler, A. Heft, W. Wesch, Nucl. Instr. and Meth. **B 141** (1998) 105.

[Wes95a] W. Wesch, A. Heft, E. Wendler, T. Bachmann, E. Glaser, Nucl. Instr. and Meth. **B 96** (1995) 335.

[Wes95b] W. Wesch, A. Heft, J. Heindl, H.P Strunk, T. Bachman, E. Glaser, E. Wendler, Nucl. Instr. and Meth. **B 106** (1995) 339.

[www1] http://www.srim.org/SRIM/Compounds.htm - 2014/01/08.

CHAPTER 7 SUMMARY AND CONCLUSIONS

Kr (360 keV) ions were implanted into 6H-SiC at three different temperatures, i.e. room temperature, 350 ^{o}C and 600 ^{o}C, up to a fluence of 2×10^{16} ions/cm^{2}. The radiation damage retained after implantation was assessed with the Rutherford backscattering technique in the channelling mode (RBS-C). Annealing of radiation damage and diffusion of the implanted Kr were investigated during isochronal annealing in the temperature range 1000 – 1500 ^{o}C in steps of 100 ^{o}C for 5 hours using RBS-C and RBS, respectively.

The room temperature implantation amorphised the 6H-SiC to a depth of approximately 280 nm from the surface. This occurred because the thermal energy of the atoms at this temperature was not high enough to allow the displaced atoms to recombine with their designated lattice positions. The high temperature implantations did not amorphise the 6H-SiC. Implantation at these temperatures did, however, cause a distortion of the 6H-SiC because of the defects and/or defect clusters that were retained. The 350 ^{o}C implantation retained a high damage density as compared to the 600 ^{o}C implantation. The reason for the decrease in damage density with increasing temperature can be explained in terms of the thermal energy available for the atoms to move around in the SiC. A high temperature implies a higher mobility of the atoms thus increasing the probability of the displaced atoms to recombine with their designated lattice positions. Consequently, a slight diffusion of the Kr was also observed at the high temperature implantations relative to the room temperature implantation. The Kr depth profiles were broader for the high temperature implantations. Since implantation at different temperatures caused different degrees of retained radiation damage in the SiC, isochronal annealing was done to assess the recovery of the SiC and also the diffusion of the implanted Kr inside the SiC under the different conditions.

Epitaxial re-crystallisation from the amorphous-crystalline interface was observed after annealing the room temperature implanted sample at 1000 ^{o}C. However, no change in the Kr depth profile was observed after annealing at 1000 and 1100 ^{o}C for 5 hours. Annealing the same sample from 1100 to 1300 ^{o}C in steps of 100 ^{o}C for

5 hours did not result in any further epitaxial re-crystallisation. There, however, was a slight change of the SiC from the surface region at 1200 ^{o}C. The Kr depth profile started to broaden slightly at 1200 ^{o}C. An increased broadening was further observed at 1300 ^{o}C. In both instances the Kr depth profiles maintained an approximately Guassian shape. This change in the Kr depth profile implies that there was Fickian type diffusion of the Kr at these temperatures. Annealing at 1400 ^{o}C resulted in a loss of about 30% of the Kr accompanied by a shift of the Kr depth profile towards the surface. These changes occurred simultaneously with the major epitaxial re-crystallisation of the SiC from the amorphous-crystalline interface. Further annealing at 1500 ^{o}C caused an additional loss of about 20% of the Kr accompanied by a pronounced shift towards the surface. This also occurred concurrently with the remarkable re-crystallization of the SiC. The Kr depth profile changes that occurred at 1400 and 1500 ^{o}C resulted in an asymmetric Kr profile and thus cannot be explained in terms of the Fickian diffusion process. The observed abrupt changes at 1400 and 1500 ^{o}C are consistent with influence of thermal etching. This is because the thermal etching effect could have influenced the RBS spectrum and resulted in asymmetric depth profiles due the surface inhomogeneity. Additionally, although there was epitaxial re-crystallisation, it is also possible that some of the amorphous material could have been partially etched away.

Unlike in the room temperature implantation case where the thermal energy had to be enough to allow (1) excess defects to escape the disordered region; (2) provide sufficient mobility to allow atomic re-ordering, and finally (3) allow for the formation of appropriate bonds, in the high temperature case there was a consistent decrease in the retained damage with each annealing cycle. Through-out the annealing cycles the 350 ^{o}C implantation retained more damage than the 600 ^{o}C implantation. In all the annealing instances there was no observable change in the Kr depth profiles implying that no diffusion took place despite the re-ordering of the displaced host (Si in our case) atoms. The stability of the Kr atoms in their implanted positions is a possible contributor to the resistance of the SiC from returning to its virgin crystalline structure as observed through the RBS-C spectrum. This is because the Kr atoms exist as point defects in the SiC lattice thus causing the de-channelling of the He ions as they penetrate the SiC. This, in addition to the de-channelling from the extended defects, caused an increased backscattering spectrum from the host atoms.

Thorough-out the entire isochronal annealing experiments in the temperature range 1000 – 1500 ^{o}C the 6H-SiC retained all of the Kr.

The results of this project indicate that volume diffusion is not significant for the migration of Kr in the TRISO particle through the SiC layer. The migration of Kr could however occur through the grain boundaries in polycrystalline SiC. Thus, further work still needs to be done to investigate grain boundary diffusion, and to determine the diffusion co-efficient of Kr in 6H-SiC/SiC. The future work will also investigate the influence swift heavy ion irradiation on the damage recovery and diffusion of Kr in both 6H-SiC and polycrystalline SiC. Several other techniques will also be used, including but not limited to scanning electron microscopy (SEM), transmission electron microscopy (TEM) and Raman spectroscopy to characterize the radiation damage recovery of SiC.